Electrochimica Acta 495 (2024) 144482

Contents lists available at ScienceDirect

Electrochimica Acta

journal homepage: www.journals.elsevier.com/electrochimica-acta

NEOPARD-X: Multidimensional highly efficient and scalable modular framework for modelling of electrolysers and fuel cells

Andrey Koksharov [a,*], Arnulf Latz [a,b], Thomas Jahnke [a,*]

[a] German Aerospace Center (DLR), Germany
[b] Helmholtz Institute Ulm for Electrochemical Energy Storage (HIU), Germany

ARTICLE INFO

Keywords:
Modelling framework
Electrolyser
Fuel cell
PEMFC
SOEC
Stack
Multidimensional

ABSTRACT

A novel framework for modelling of electrolysers and fuel cells is presented. The framework features a modular and flexible structure, which enables wide applicability for a variety of fuel cell and electrolyser technologies. The framework is multi-threaded for shared memory architectures. The generic approach for discretisation allows efficient distribution of tasks between processing cores. The physical model is clearly separated from discretisation and the linear solver. This simplifies the model development and provides high flexibility with respect to the discretisation methods, linear solvers, as well as the dimensionality of the application. Irregular grids and complex geometries can be realised through generic mapping of coordinate systems. Single cell models can be easily scaled to short stacks. The framework features are demonstrated with realistic PEMFC and SOEC models. Whilst the PEMFC example focuses on the differences between different model dimensions and different boundary conditions, the SOEC example demonstrates the extension of a transient single cell model to a transient short stack model. The performance scalability with the number of CPUs is demonstrated.

1. Introduction

Electrolysers and fuel cells play an essential role in the transition to a green hydrogen economy. Therefore, the development and improvement of various electrolyser and fuel cell technologies are subject of current research. Two promising examples of these technologies are based on solid oxide (SO) and proton exchange membrane (PEM) electrolytes. SO and PEM cells consist of different materials and have different working principles: one is based on an ion conducting electrolyte operating at high temperatures around 800 °C and the other is based on a proton conducting membrane operating at temperatures typically below 100 °C. Nevertheless, when considering the processes on cell or stack level they have common governing equations describing mass, charge and energy transport coupled with electrochemical reactions (see Section 3).

Fuel and electrolyser cells based on SO and PEM are modelled extensively over several decades [1–3]. A number of models were developed ranging from zero-dimensional (0D) to three-dimensional (3D) at different length scales. There are in general 3 model levels: stack level, cell level and microscopic level. Stack level models couple complex fluid dynamics with heat transfer and simplified chemical models to assist system design, see e.g. [4–7]. Cell level models study flow and chemistry within porous composite electrodes. These models may include the gas and liquid phase species transport through the pore phase, surface diffusion of adsorbed species, the charge transport within the ionic and electronic conducting phases, charge balance, and charge-transfer kinetics. However the internal microscopic structure is not resolved up to the single pores, see e.g. [8–11]. The microscopic models focus on specific process, i.e. transport processes in the gas diffusion layer (GDL) or charge transfer processes in the catalyst layer (CL), and resolve the microscopic structure in the region of interest in the fuel cell. Microscopic models are mostly attributed to direct numerical simulations (DNS) or Lattice Boltzmann methods (LBM), see e.g. [12–14] correspondingly. A comprehensive review of the modelling approaches can be found in [15,16].

By increasing the dimensionality of the model, more information is gained on properties distribution such as temperature or electrical potential but it often comes at the cost of accuracy of the model description. Multidimensional models (2D or 3D) incorporate the global Butler–Volmer kinetic and often apply zero-dimensional description of the electrolyte, or focus on specific phenomena [15,16]. The limitations of global Butler–Volmer approach compared to elementary kinetics, particularly that the required Nernst potential is not available at non-equilibrium, is described in [17]. Additionally, multidimensional cell models are commonly built on top of an existing computational fluid dynamics (CFD) software, e.g. ANSYS FLUENT, COMSOL or OpenFOAM. In addition, a few open source frameworks have been developed

---

* Corresponding authors.
E-mail addresses: andrey.koksharov@dlr.de (A. Koksharov), thomas.jahnke@dlr.de (T. Jahnke).

https://doi.org/10.1016/j.electacta.2024.144482
Received 4 December 2023; Received in revised form 8 May 2024; Accepted 21 May 2024

Nomenclature

ξ	numerical coordinate
η	Overpotential, V
Γ	Site density, mol/m^3, mol/m^2 or mol/m
κ	Heat conductivity, W/K/m
λ	Water content
$\mathbf{f}$	General flux term
$\mathbf{g}$	Gravitational acceleration, m/s^2
$\mathbf{i}_{\mathrm{el}}$	Electronic current density, A/m^2
$\mathbf{i}_{\mathrm{ion}}$	Ionic or protonic current density, A/m^2
$\mathbf{n}$	Normal vector to boundary
$\mathbf{v}$	Gas velocity, m/s
$\mathbf{x}$	physical (model) coordinate
$\mathcal{D}_{ij}$	Binary diffusion coefficient, m^2/s
$\mathcal{F}$	Faraday constant, C/mol
$\mathcal{R}$	Molar gas constant, J/mol/K
ν	Stoichiometric coefficient
$\overline{h}$	Molar enthalpy, J/mol
$\overline{s}$	Molar entropy, J/mol/K
ρ	Mass density, kg/m^3
σ_{el}	Electronic conductivity, S/m
σ_{ion}	Ionic or protonic conductivity, S/m
ε_{g}	Gas phase weight (porosity), m^3/m^3
ε_i	Phase weight, m^3/m^3, m^2/m^3 or m/m^3
φ_{el}	Electronic potential, V
φ_{ion}	Ionic or protonic potential, V
c	Molar concentration, mol/m^3, mol/m^2 or mol/m
D_{ij}	Diffusion coefficient, m^2/s
G	Gibbs free energy, J/mol
K	Permeability, m^2
k_i	Knudsen diffusion coefficient, m^2/s
M_i	Molar mass of species i, kg/mol
p	Pressure, Pa
q	General source term
s	General storage term
T	Temperature, K
X	Mole fraction

particularly for multidimensional fuel cell models [18,19]. In the case of the commercial software, the CFD basis is a black box with limited adjustment possibilities. Even in the case of openly available code like OpenFOAM, the adjustment in the code with over million lines is not a trivial task.

The aim of this work is to develop a computationally efficient, modular and flexible framework for simulations of fuel and electrolyser cells at the cell level using a volume-averaged approach. The computations can be performed for transient as well as stationary applications. The work is based on the previously developed framework NEOPARD-X (Numerical Environment for the Optimisation of Performance And Reduction of Degradation of X (= energy conversion device)) [20–23].

Over the past two years, the framework was significantly rewritten in order to increase the flexibility and the computational efficiency. The main limitation of the previous version was the computing on a single CPU, which resulted in long computation times for complex models. The second limitation, which is also common to many other models, is direct coupling of the model equations and the discretisation, e.g. finite volumes method. The cell models are rapidly evolving and the manual discretisation of governing equations limits the code flexibility.

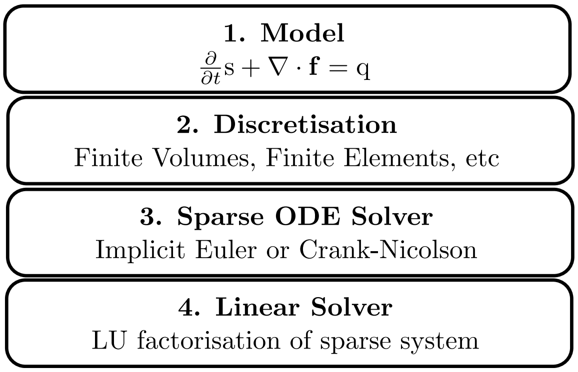

Fig. 1. Framework hierarchy.

The new NEOPARD-X framework ver. 2.0 has a modular structure, which allows switching electro-chemical models, molecular transport models or modify/extend existing models for specific applications. Although current applications have a relatively simple rectangular geometry, more complex curved cell geometries, e.g. graded electrodes, can be studied with intrinsic coordinate transformations. In this paper the discussion is limited to 1D and 2D cases but the framework is generally applicable also to three dimensions.

The main purpose of the framework is a rapid model development in the area of fuel and electrolyser cells. The framework features a new approach to the separation of the numerical discretisation and the mathematical model. This permits a simple change of the model dimensions and geometry, as well as effective performance scalability on modern CPU. Additionally, it permits straightforward extension of a cell model to a stack model.

This article has the following structure: in Section 2 an overview of the cell modelling framework is given; Section 3 describes standard modules for the mathematical description of the cell models; Section 4 provides an example for a PEMFC and a SOEC model.

2. Framework structure

The main idea of the framework is to separate the physical model description from the numerics, i.e. the discretisation method and the solver. This allows applying different discretisation schemes for the same model and to focus more on model development. For this reason the framework has the following hierarchical structure (Fig. 1).

On the upper level (1) the system of model equations is provided. On the lower level (2) the system is discretised in space. On the level (3) the system is solved iteratively for each time step. The lowest level (4) is required for the solution of the resulting linear system for each iteration step.

2.1. Model level

Each mathematical domain is enclosed by domains of lower dimension (see Fig. 2). Consider e.g. 2D domain (1), which boundary condition represent 1D domains (3),(4),(6) and (8). The domain (3) has two 0D boundaries (10) and (13), whilst the domain (4) has boundaries (11) and (14).

Each domain m is governed by a set of partial differential equations of the form

$$\frac{\partial}{\partial t}s^m + \nabla \cdot \mathbf{f}^m = q^m, \tag{1}$$

where

$$\begin{aligned} s &= s\left(u^m,\ \partial u^m/\partial \mathbf{x}^m,\ \mathbf{n}^{k,m} \cdot \partial u^k/\partial \mathbf{x}^k\right), \\ \mathbf{f} &= \mathbf{f}\left(u^m,\ \partial u^m/\partial \mathbf{x}^m,\ \mathbf{n}^{k,m} \cdot \partial u^k/\partial \mathbf{x}^k\right), \\ q &= q\left(u^m,\ \partial u^m/\partial \mathbf{x}^m,\ \mathbf{n}^{k,m} \cdot \partial u^k/\partial \mathbf{x}^k\right) \end{aligned}$$

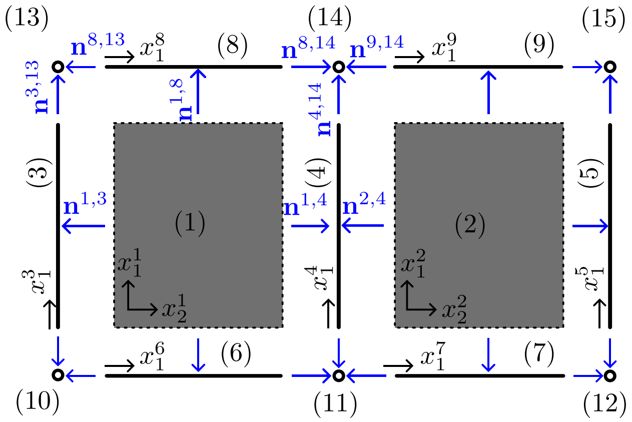

Fig. 2. Exemplary 2D domain relations: (i) represents numerical domain i, $n^{i,j}$ is the normal vector to domain i at the boundary domain j, x_k^i is the direction of the coordinate vector k in the numerical domain i.

are the storage, flux and source terms correspondingly. These terms are the user defined functions describing the model.

Here the first parameter u^m is the state variable in the domain m, second is gradient of the state variables in respect to domain coordinates x_i^m. The last parameter requires a special attention. It represents the projection of state variable in domain k to normal vector in respect to boundary m. E.g. for domains (1) and (2) in Fig. 2 this term is absent but for domain (4) there are two terms $\sum_{j=1}^{2} n_j^{1,4}\,\partial u^1/\partial x_j^1$ and $\sum_{j=1}^{2} n_j^{2,4}\,\partial u^2/\partial x_j^2$. This parameter is required for Neumann type of boundary and coupling conditions.

Note that for corner points (10) through (15) the corresponding domains are 0D and Eq. (1) is reduced to

$$\frac{\partial}{\partial t} s^m = q^m, \tag{2}$$

The discussion in this work is limited to 2D for simplicity of representation but the framework is applicable for arbitrary high dimensions. E.g. a 3D domain is enclosed by 6 2D domains, which are in turn enclosed by 4 1D domains and so on.

2.2. Space discretisation level

In general there are 2 types of grid points, which are independent from the discretisation method (s. Fig. A.15):

1. Points x_i^m, where the state variables u_i^m are estimated;
2. Points $\tilde x_i^m$, where equation components $\tilde s_i^m$, $\tilde{\mathbf{f}}_i^m$ or $\tilde q_i^m$ are approximated.

Points x_i^m and $\tilde x_i^m$ are generated automatically, depending on grid vertex points provided by the user (see Appendix A for more details).

The aim of the discretisation is not only to create an approximation of the Eq. (1) but also to create interpolation relations of state variables between points x_i^m and $\tilde x_i^m$.

1. Interpolation of a state variable is a weighted sum of states across domains k
$$\tilde u_i^m = \sum_k \sum_j a_{i,j}^{m,k}\, u_j^k, \tag{3}$$
where $\tilde u_i^m$ is the interpolated value at point $\tilde x_i^m$ and $a_{i,j}^{m,k}$ is the weight of point x_j^k.
2. Gradient of a state variable at point $\tilde x_i^m$ is also a weighted sum of states across domains k
$$\frac{\partial}{\partial \mathbf{x}^m}\tilde u_i^m = \sum_k \sum_j \mathbf{b}_{i,j}^{m,k}\, u_j^k, \tag{4}$$
where $\mathbf{b}_{i,j}^{m,k}$ is the vector weight of point x_j^k.
3. Normal gradient to the boundary, in the higher dimensional domain n is
$$\mathbf{n}^{n,m}\cdot\frac{\partial}{\partial \mathbf{x}^n}\tilde u_i^m = \sum_k \sum_j c_{i,j}^{m,k}\, u_j^k, \tag{5}$$
where $\mathbf{n}^{n,m}$ is normal vector to the boundary m in domain n and $c_{i,j}^{m,k}$ is the weight of point x_j^k.
4. Time dependent discrete (ODE) form of Eq. (1) in domain m for point x_i^m
$$\sum_j \alpha_{i,j}^m \frac{\partial}{\partial t}\tilde s_j^m \;+\; \boldsymbol{\beta}_{i,j}^m\cdot\tilde{\mathbf{f}}_j^m = \sum_j \gamma_{i,j}^m\,\tilde q_j^m, \tag{6}$$
where
$$\begin{aligned}\tilde s_i^m &= s\left(\tilde u_i^m,\ \partial\tilde u_i^m/\partial\mathbf{x}_i^m,\ \mathbf{n}^{k,m}\cdot\partial\tilde u_i^k/\partial\mathbf{x}_i^k\right),\\ \tilde{\mathbf{f}}_i^m &= \mathbf{f}\left(\tilde u_i^m,\ \partial\tilde u_i^m/\partial\mathbf{x}_i^m,\ \mathbf{n}^{k,m}\cdot\partial\tilde u_i^k/\partial\mathbf{x}_i^k\right),\\ \tilde q_i^m &= q\left(\tilde u_i^m,\ \partial\tilde u_i^m/\partial\mathbf{x}_i^m,\ \mathbf{n}^{k,m}\cdot\partial\tilde u_i^k/\partial\mathbf{x}_i^k\right)\end{aligned}$$
are storage term, flux and source approximations respectively. Coefficients α, $\boldsymbol{\beta}$ and γ are weights of points $\tilde x_i^m$.

In other words, the aim of the discretisation is to provide the coefficients $a_{i,j}^{m,k}$, $\mathbf{b}_{i,j}^{m,k}$, $\alpha_{i,j}^m$, $\boldsymbol{\beta}_{i,j}^m$ and $\gamma_{i,j}^m$. Because only non-zero coefficients are stored, the local residual at each collocation point can be computed independently with limited interaction with neighbours.

An example of a discretisation with face centred finite volumes (FCFV) method is shown in Appendix A. This method is of second order on equidistant grids. Although the current discussion is limited to FCFV method, the approach is generally applicable to other discretisation methods.

2.3. ODE level

Eq. (6) represents an ODE system with interconnectivity between elements (depends on discretisation). Due to the stiffness of the electrochemical application the implicit Euler O(1) and Crank–Nicolson O(2) are chosen for the framework. The fully discretised semi linear system takes the following form for a single time step $h = t_1 - t_0$

$$\begin{aligned}&\sum_j \alpha_{i,j}^m\left(\tilde s_j^m(t_1) - \tilde s_j^m(t_0)\right)\\ &\quad + h\,\boldsymbol{\beta}_{i,j}^m\cdot\left(\tau_1\,\tilde{\mathbf{f}}_j^m(t_1) \;-\; \tau_0\,\tilde{\mathbf{f}}_j^m(t_0)\right)\\ &\quad - h\,\gamma_{i,j}^m\left(\tau_1\,\tilde q_j^m(t_1) \;-\; \tau_0\,\tilde q_j^m(t_0)\right)\\ &\quad = 0,\end{aligned} \tag{7}$$

where brackets (t_0) and (t_1) indicate the initial condition at time t_0 and the sought solution at the time t_1 respectively. The coefficients τ depend on the applied method:

- Implicit Euler: $\tau_1 = 1$, $\tau_0 = 0$,
- Crank–Nicolson: $\tau_1 = 1/2$, $\tau_0 = 1/2$.

For more information on the above time integration methods the reader is referred to standard textbooks, e.g. [24].

If in Eq. (1) the storage term is absent

$$\nabla\cdot\mathbf{f}^m = q^m, \tag{8}$$

the discrete form is computed through

$$\boldsymbol{\beta}_{i,j}^m\cdot\tilde{\mathbf{f}}_j^m(t_1) - \gamma_{i,j}^m\,\tilde q_j^m(t_1) = 0. \tag{9}$$

A set of Eqs. (7) and (9) for one grid point represent one computational unit. Coefficients a, $\mathbf{b}$, α, $\boldsymbol{\beta}$ and γ describe relations with other computational units. Thus each computational unit can reconstruct the local residual and the corresponding row of the global Jacobian matrix independently. A straightforward parallelisation can be done by distributing equally these units across processor cores. However, due to the heterogeneous nature of the processes in fuel and electrolyser

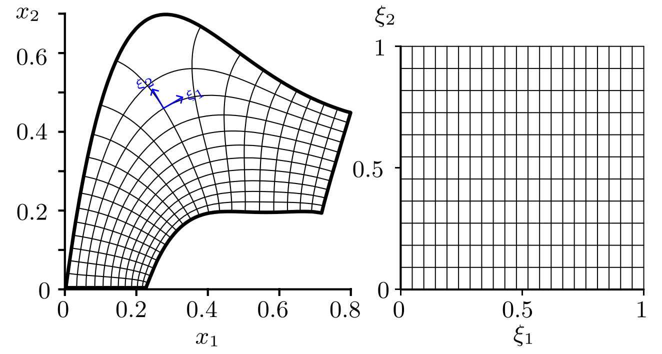

Fig. 3. Exemplary coordinate map: left — physical domain, right — numerical domain.

cells, the number equations and the efforts to compute one equation may vary significantly, resulting in idle cores. For this reason the computational units are combined into small batches which are put on the job heap. Parallel jobs are taking task from the heap. The process is governed by the total number of unknowns for each batch M. The number M may vary depending on the physical model.

2.4. Linear solver and time step adaptation

Eq. (7) is solved iteratively with the Newton Method (see e.g. [24]). For the solution, the terms $\tilde{s}_j^m(t_1)$, $\tilde{\mathbf{f}}_j^m(t_1)$ and $\tilde{q}_j^m(t_1)$ are linearised around the current solution estimate and the required Jacobian matrices of these terms are computed numerically once for each time step. This results in a sparse linear system, which can be solved with various solvers, e.g. SuperLU [25] or Intel® oneAPI PARDISO.

Newton iterations are continued until the residual R for each equation Eq. (7) or (9) is smaller than the tolerance TOL

$$R < \mathrm{TOL}. \tag{10}$$

The residual is computed as LHS of Eq. (7).

If the desired tolerance cannot be reached within the maximum allowed number of iterations, the time step size is halved. By reaching the condition Eq. (10), the next time step h_1 is determined through

$$h_1 = h_0 \left(\frac{N}{N_{\text{target}}}\right)^{-\alpha}, \tag{11}$$

with N and N_{target} denoting actual and desired number of iterations respectively. The damping parameter α is typically chosen $0.1 \le \alpha \le 0.5$, with lower value required for impedance calculations, whereas upper value is sufficient for steady state approximations.

2.5. Irregular grids and curved domains

Rectangular representation of physical domains, as shown in Fig. 2, limits the application range. A generic domain mapping aims to extend the framework to more complex domain configurations.

Fig. 3 shows an example of mapping of a physical domain (left) to the corresponding numerical domain (right)

$$\mathbf{x} = \mathbf{x}(\xi). \tag{12}$$

Computations are performed on an equidistant grid with coordinates $\xi_i \in [0, 1]$. It is straightforward to show (see e.g. [26]) that Eq. (1) is equivalent to[1]

$$\frac{\partial}{\partial t}(g\, s^m) + \nabla_\xi \cdot \left(\mathrm{adj}(J) \cdot \mathbf{f}^m\right) = g\, q^m, \tag{13}$$

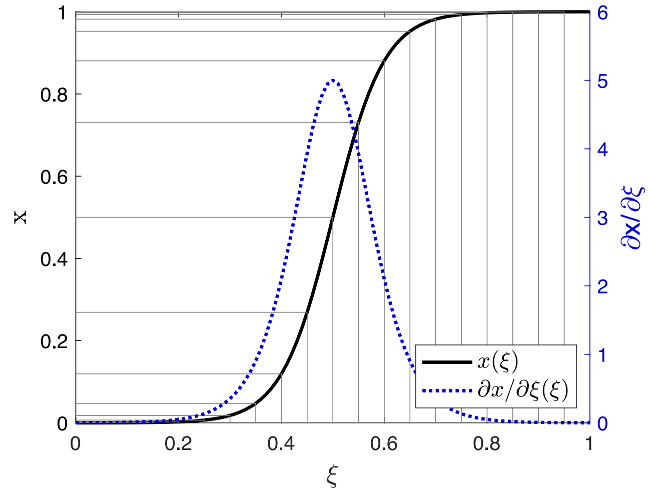

Fig. 4. Sigmoid coordinate transformation for $a = 0.1$ and $b = 0.5$.

where $\nabla_\xi \cdot \mathbf{v} = \sum_i \partial v_i/\partial \xi_i$ is divergence operator in $\boldsymbol{\xi}$ domain; $g = \det(J)$ is the determinant of the transformation Jacobian matrix J, which is defined as

$$J = \frac{\partial \mathbf{x}}{\partial \xi}. \tag{14}$$

In the framework, the components of the Jacobian $\partial x_i/\partial \xi_j$ in Eq. (14) can be either provided (e.g. if the transformation is analytical) or computed automatically with second order piecewise polynomial.

2.5.1. Domain stretching

One of the possible application of irregular grids is domain stretching/contracting, e.g. adding more discretisation points (in physical coordinates) near domain boundaries. In numerical experiments the largest changes of state variables were observed near the layer interfaces and at the domain boundaries. For this reason more grid points are required near the boundaries, which is represented by the sigmoid transformation function (compare Eq. (12))

$$x_i = d_i + \frac{c_i}{1 + \exp\left(\left(b_i - \xi_i\right)/a_i\right)}, \quad \forall\, i = 1,\, 2. \tag{15}$$

The coefficients a_i and b_i depend on specific problem and describe the location and the "width" of the sigmoid step respectively. The coefficients c_i and d_i are computed to fulfil the condition at the left boundary $x_{1,0} = x_1(0)$ and at the right boundary $x_{1,\infty} = x_1(1)$.

The components of coordinate transformation Jacobian (14) for the sigmoid stretch, when applied for each coordinate, takes the following recursive form

$$\frac{\partial x_i}{\partial \xi_j} = \begin{cases} \dfrac{x_i - d_i}{a_i}\left(1 - \dfrac{x_i - d_i}{c_i}\right), & \forall\, i = j, \\ 0, \quad \forall\, i \ne j, \end{cases} \tag{16}$$

where $x_i = x_i(\xi)$ according to Eq. (15).

A typical sigmoid transformation function is illustrated in Fig. 4. Equidistantly distributed points within numerical coordinates ξ are located more dense near boundaries in physical coordinates x.

---

[1] i.e. in 1D: $g = \frac{\partial x}{\partial \xi}$, $\frac{\partial}{\partial t}(g\, s^m) + \frac{\partial}{\partial \xi} f^m = g\, q^m$, in 2D: $g = \frac{\partial x_1}{\partial \xi_1}\frac{\partial x_2}{\partial \xi_2} - \frac{\partial x_1}{\partial \xi_2}\frac{\partial x_2}{\partial \xi_1}$, $\frac{\partial}{\partial t}(g\, s^m) + \frac{\partial}{\partial \xi_1}\left(\frac{\partial x_2}{\partial \xi_2} f_1^m - \frac{\partial x_1}{\partial \xi_2} f_2^m\right)$ $+ \frac{\partial}{\partial \xi_2}\left(\frac{\partial x_1}{\partial \xi_1} f_2^m - \frac{\partial x_2}{\partial \xi_1} f_1^m\right) = g\, q^m$.

.

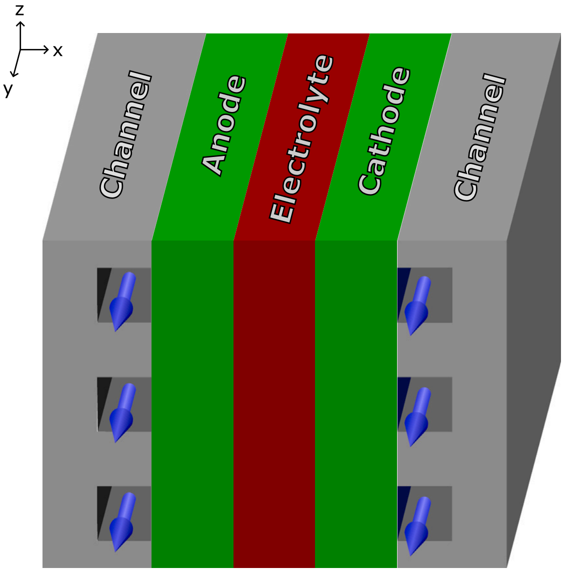

Fig. 5. Schematic representation of a cell model.

3. Building block for cell models

The overall model of an electrolyser or fuel cell consist of an arbitrary number of layers. Fig. 5) shows a simplified cell model with 5 layers (from left to right): fuel channel, fuel electrode, electrolyte, air electrode and air channel. The electrodes themselves can consist of several layers, e.g. catalyst layers and gas diffusion layers.

The volume averaged model for each layer assumes a number of phases homogeneously mixed together. There are fluid phase, bulk (solid) and interface phases (double phase, triple phase boundaries). Each phase i has its own weight ε_i in the model, which has different physical meaning

- Fluid and bulk phases: ε_i / $\mathrm{m}^3/\mathrm{m}^3$;
- Double phase boundary: ε_i / $\mathrm{m}^2/\mathrm{m}^3$;
- Triple phase boundary: ε_i / m/m^3.

Within each layer there are in general 4 equation blocks: momentum, energy, species and charge conservation (see Table 1). The block for momentum represents 2 alternative models (Darcy and Darcy–Brinkman), which can be used for the resolution of the velocity field $\mathbf{v}$. The choice of the model depends on the application. Whereby, the Darcy–Brinkman equation Eq. (18) (see Table 1) is automatically reduced to Navier–Stokes equation with porosity $\varepsilon_\mathrm{g} \rightarrow 1$ and the permeability $K \rightarrow \infty$.

Multiple state variables are possible in the layer model, i.e. velocity field $\mathbf{v}$, temperature T, species molar concentration c_j, ionic potential φ_ion, electronic potential φ_el, etc.

Depending on dimensionality of the model different configurations are possible. The 1D model resolves the dimension through the thickness of the cell. For 2D models there are 2 possible configurations, see Fig. 6. One is the slice along the gas channel and the other one is the slice orthogonal (through) channel. The latter case assumes the equal gas flow in the supply channels, which allows to study only one portion of the cell with appropriate symmetry boundary conditions.

3.1. Energy conservation

The energy block Eq. (19) represents the first law of thermodynamics. The conserved internal energy pro unit volume of each phase u_i is computed according to

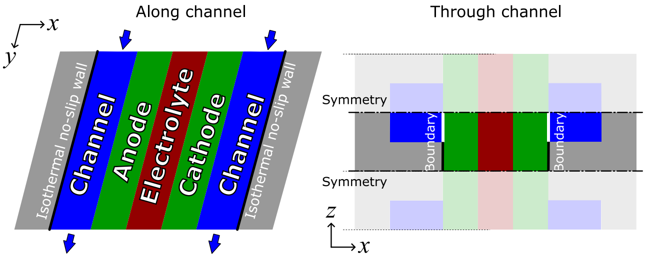

Fig. 6. 2D model configurations.

- Fluid (gas) phase:

$$u_\mathrm{g} = \sum_{j\in \mathrm{g}} c_j \overline{h}_j - p, \tag{33}$$

  whereby the kinetic energy is neglected due to relatively slow flows in electrolyser and fuel cells;
- Bulk phase j: $u_i = h_i = h_i(T)$, where h_i is a user defined function for mass specific enthalpy;
- Interface phase: $u_i = 0$.

The effective heat conductivity is estimated as a weighted mixture of heat conductivities κ_i and heat resistivities κ_i^{-1} (mixture of series and parallel circuits) of corresponding phases

$$\kappa_\mathrm{eff} = \frac{1}{2}\left(\sum_i \varepsilon_i \kappa_i + \left(\sum_i \frac{\varepsilon_i}{\kappa_i}\right)^{-1}\right) \tag{34}$$

Heat conductivity depends on phase type

- Gas phase [27]:

$$\kappa_\mathrm{g} = \frac{1}{2}\left(\sum_{j\in \mathrm{g}} X_j \kappa_j^\mathrm{g} + \left(\sum_{j\in \mathrm{g}} \frac{X_j}{\kappa_j^\mathrm{g}}\right)^{-1}\right), \tag{35}$$

  where κ_j^g is the heat conductivity of gas, containing only the species j, with mole fraction X_j;
- Bulk phase: $\kappa_i = \kappa_i(T)$, where $\kappa_i(T)$ is a user defined function.
- Interface phase: $\kappa_i = 0$, i.e. heat conductivity along interfaces between phases is neglected.

3.2. Molecular transport

In its most general form the molecular transport is assumed in the form of Nernst–Planck equation (see Eqs. (28)). It is governed by effective diffusion coefficients D_{ij}. These coefficients are computed according to the following expression, which is adapted from [28]

$$D_{ij} = d_j\left(\delta_{ij} - M_j \frac{c_i}{\rho} - X_i\right) + c_i \sum_k \rho_k d_k, \tag{36}$$

where δ_{ij} is Kronecker delta function and d_j are coefficients diffusion coefficients for the flux equation of the form

$$\mathbf{j}_j = d_j \nabla X_j. \tag{37}$$

Essentially the Eq. (36) is the conversion from mole fractions X_i to molar concentrations c_i, ensuring the mass conservation

$$\sum_i M_i \mathbf{j}_i = 0. \tag{38}$$

Hereby M_i is the molar mass of species i.

The framework currently considers two ways of estimating diffusion coefficients

- Bulk diffusion: if one component is in excess

$$d_i = -\frac{\varepsilon}{\tau^2}\left(\frac{1}{\mathcal{D}_{i,n}} + \frac{1}{k_i}\right)^{-1}, \tag{39}$$

Table 1
Summary of layer models.

Model		Storage	Flux	Source	
Momentum	Darcy	0	0	$\mathbf{v}+(\nabla p-\rho\mathbf{g})\,\frac{K}{\mu}$	(17)
	Darcy-Brinkman	$\varepsilon_{\mathrm{g}}\rho\mathbf{v}$	$\varepsilon_{\mathrm{g}}\,(\rho\mathbf{v}\otimes\mathbf{v}+\mathbf{T}+\mathbf{S})$	$\varepsilon_{\mathrm{g}}\left(\rho\mathbf{g}-\nabla p-\mathbf{v}\frac{\mu}{K}\right)$	(18)
	Energy	$\sum_{\alpha\in\Phi}\varepsilon_\alpha u^\alpha$	$\varepsilon_{\mathrm{g}}\left(\mathbf{v}\sum_{j\in\mathrm{g}}c_j\overline{h}_j+\mathbf{T}\cdot\mathbf{v}\right)+\sum_{j\in S}\bar{\mathbf{j}}_j\overline{h}_j-\kappa_{\mathrm{ef}}\nabla T$	$\mathbf{i}_{\mathrm{el}}\cdot\nabla\varphi_{\mathrm{el}}+\mathbf{i}_{\mathrm{ion}}\cdot\nabla\varphi_{\mathrm{ion}}-\overline{q}_{\mathrm{el}}\mathcal{F}\Delta\varphi$	(19)
Species j	Gas phase g	$\varepsilon_{\mathrm{g}}c_j$	$\mathbf{v}\varepsilon_{\mathrm{g}}c_j+\bar{\mathbf{j}}_j$	$\overline{q}_j$	(20)
	Other phase α	$\varepsilon_\alpha c_j$	$\bar{\mathbf{j}}_j$	$\overline{q}_j$	(21)
Potential	Ionic	$-C_{\mathrm{dl}}\Delta\varphi$	$\mathbf{i}_{\mathrm{ion}}$	$-\mathcal{F}\,\overline{q}_{\mathrm{el}}$	(22)
	Electron	$C_{\mathrm{dl}}\Delta\varphi$	$\mathbf{i}_{\mathrm{el}}$	$\mathcal{F}\,\overline{q}_{\mathrm{el}}$	(23)
	Ionomer water[a]	$\varepsilon_\alpha\frac{\rho_{\mathrm{dry}}}{\mathrm{EW}}\frac{\partial\lambda}{\partial t}$	$n_{\mathrm{d}}\frac{\sigma}{F}\nabla\varphi_{\mathrm{ion}}+\frac{\rho_{\mathrm{dry}}}{\mathrm{EW}}D_\lambda^{\mathrm{eff}}\nabla\lambda$	q_λ	(24)

[a] Used in PEM models only.

Table 2
Closing expressions for layer models.

Shear stress	$\mathbf{T}=diag\left(\frac{2}{3}\mu\nabla\cdot\mathbf{v}\right)-\mu\left(\nabla\mathbf{v}+(\nabla\mathbf{v})^T\right)$	(25)
Eddy viscosity	$\mathbf{S}=-\rho\,\nu_{\mathrm{eddy}}\left(\nabla\mathbf{v}+(\nabla\mathbf{v})^T\right)$	(26)
Pressure	$p=\mathcal{R}T\sum_{j\in\mathrm{g}}c_j$	(27)
Species flux	$\bar{\mathbf{j}}_j=\sum_k D_{jk}\left(\nabla c_k+\frac{\mathcal{F}}{\mathcal{R}T}z_k c_k\nabla\varphi_{ion}\right)$	(28)
Ionic current (a)	$\mathbf{i}_{\mathrm{ion}}=\mathcal{F}\sum_j\bar{\mathbf{j}}_j\,z_j$	(29)
Ionic current (b)	$\mathbf{i}_{\mathrm{ion}}=-\sigma_{\mathrm{ion}}\nabla\varphi_{\mathrm{ion}}$	(30)
Electronic current	$\mathbf{i}_{\mathrm{el}}=-\sigma_{\mathrm{el}}\nabla\varphi_{\mathrm{el}}$	(31)
Potential step	$\Delta\varphi=\varphi_{\mathrm{el}}-\varphi_{\mathrm{ion}}$	(32)

where n is index of species in excess, ε is the phase weight, τ is the tortuosity of the phase and k_i defines Knudsen diffusion coefficient.

- Mixture averaged [28]

$$d_i=\frac{\varepsilon}{\tau^2}c\left(\frac{M_i c_i}{\rho}-1\right)\left(\frac{c}{k_j}+\sum_j\frac{c_j}{\mathcal{D}_{ij}}\right)^{-1}. \tag{40}$$

Evidently the Knudsen diffusion is applicable for the gas phase only. In the latter case the Knudsen diffusion coefficient is approximated according to [29]

$$k_i=\frac{2}{3}r_{\mathrm{p}}\sqrt{\frac{8\mathcal{R}}{\pi}\frac{T}{M_i}}, \tag{41}$$

where r_{p} is the mean pore radius.

In the case of the gas phase, the binary diffusion coefficients are computed according to gas kinetic theory (see e.g. [30,31]). In the case of a bulk phase, a temperature dependent function $\mathcal{D}_{ij}=\mathcal{D}_{ij}(T)$ must be provided.

Species flux Eq. (28) is a general equation for charge and uncharged species. Should a species have no charge $z_k=0$, the Nernst–Planck equation is reduced to Fick's diffusion.

3.3. Chemical source term

The source term in species conservation Eqs. (20) and (21) describes the volume production of species, which can be computed either from Butler–Volmer or elementary kinetics relations.

3.3.1. Butler–Volmer kinetics

The Butler–Volmer equation (BV) describes the relation between the overpotential η and the current j_r produced by the electrochemical reaction r

$$j_r=j_{0,r}\left(\exp\left(\frac{z_r\alpha^{\mathrm{f}}\mathcal{F}}{\mathcal{R}T}\eta_r\right)-\exp\left(-\frac{z_r\alpha^{\mathrm{b}}\mathcal{F}}{\mathcal{R}T}\eta_r\right)\right)\times\prod_{j\in S}\left(\frac{c_j}{c_{0,j}}\right)^{\beta_{r,j}}, \tag{42}$$

here z_r is the electrons produced during the reaction r, S is the set of all species. The cathodic transfer coefficient α^{f} is typically related to anodic transfer coefficient $\alpha^{\mathrm{b}}=1-\alpha^{\mathrm{f}}$ but it can be set independently for complex reactions. The overpotential is defined as

$$\eta_r=\Delta\varphi-U_{0,r}, \tag{43}$$

where $U_{0,r}$ is equilibrium voltage for reaction r.

The reaction current is related to the species production $\overline{q}_i$ by

$$\overline{q}_i=\frac{1}{\varepsilon_i}\sum_{r\in R}\varepsilon_r\,\nu_{r,i}\,\frac{j_r}{z_r\mathcal{F}}, \tag{44}$$

where z_r is the charge produced by the reaction r, $\nu_{r,i}$ is the stoichiometric coefficient for species i in the reaction r and R represents the set of all reactions.

3.3.2. Elementary kinetics

Alternatively to the BV approach, the chemical source terms in the mass continuity Eqs. (20) and (21) can also be described by elementary kinetics in the following form (see e.g. [28,32])

$$\overline{q}_i=\frac{1}{\varepsilon_i}\sum_{r\in R}\varepsilon_r\,\nu_{r,i}\left(k_r^{\mathrm{f}}\prod_{j\in S}c_j^{\nu'_{r,j}}-k_r^{\mathrm{b}}\prod_{j\in S}c_j^{\nu''_{r,j}}\right), \tag{45}$$

where ε_r and ε_i is the weight of the reaction phase and of the species phase respectively, e.g. porosity for the gas phase. Here $\nu_{r,i}=\nu''_{r,i}-\nu'_{r,i}$, with $\nu'_{r,i}$ and $\nu''_{r,i}$ are representing stoichiometric coefficients of educts and products in the reaction r respectively. Here R represents the set of all reactions and S is the set of all species. If third-bodies M are involved[2] in reaction r, the production rate for this reaction is multiplied by an efficient third-body concentration:

$$[M]_r=\sum_{i\in S}\alpha_{r,i}c_i. \tag{46}$$

where $\alpha_{r,i}$ is enhanced third-body collision efficiency of species i for reaction r.

There are two approaches for calculation of forward rate constants k_r^{f}.

---

[2] Used in gas phase reactions, e.g. $\mathrm{H}+\mathrm{OH}+\mathrm{M}\longleftrightarrow\mathrm{H_2O}+\mathrm{M}$.

3.3.3. Sticking formulation

Adsorption of a species i at the interface between gas and a solid phase ω is described through

$$k_r^{\mathrm{f}} = \frac{S_i}{\Gamma_\omega^m}\sqrt{\frac{\mathcal{R}T}{2\pi M_i}}, \tag{47}$$

where S_i is the sticking coefficient, Γ_ω is the site density of the interface phase ω and

$$m = \sum_{j\in\alpha_r} \nu'_{r,j} \tag{48}$$

is the sum of stoichiometric coefficients of species in reaction r, which belong to the same phase α_r as the reaction.

N.B. Within the framework the sticking formulation is not applicable for charge transfer reactions.

3.3.4. Arrhenius formulation

The rate constant of a general elementary reaction can be modelled with the following expression

$$k_r^{\mathrm{f}} = A_r^*\, T^{b_r} \exp\left(-\frac{E_r^*}{\mathcal{R}T}\right), \tag{49}$$

where the pre-exponential factor for reaction r may depend on the surface coverage θ_j

$$A_r^* = A_r \prod_{j\in S} \theta_i^{\mu_{r,j}}. \tag{50}$$

The effective activation energy depends on surface potential $\Delta\varphi$ and surface coverage θ_j

$$E_r^* = E_r + \alpha^*\, \mathcal{F} z_r \Delta\varphi + \sum_{j\in S} \epsilon_{r,j}\theta_j, \tag{51}$$

where $\alpha^* \in (0,1)$ is charge transfer coefficient, which is related to cathodic transfer coefficient α (see e.g. [33,34])

$$\alpha^* = \begin{cases} \alpha, & \text{if} \quad \mathrm{Red} \rightarrow \mathrm{Ox} + z''\,\mathrm{e}^- \\ (1-\alpha), & \text{if} \quad \mathrm{Ox} + z'\,\mathrm{e}^- \rightarrow \mathrm{Red} \end{cases} \tag{52}$$

The charge transfer coefficient is by default $\alpha^* = 0.5$, if not otherwise specified

The number of electrons transferred $z_r = z''_r - z'_r$ in Eq. (51) depends on reaction type: oxidation reactions $z_r > 0$, reduction reactions $z_r < 0$ and reactions without charged particles $z_r = 0$.

A care should be taken about the sign of the correction for activation energy $\epsilon_{r,j}$ in Eq. (51). An alternative formulation[3] with negative sign is present in the literature, see e.g. [35,36].

3.3.5. Reverse reaction rates

Rates of reverse reactions k_r^{b} are computed from the thermodynamic equilibrium.

$$\frac{k_r^{\mathrm{b}}}{k_r^{\mathrm{f}}} = \exp\left(-\frac{\Delta G_r}{\mathcal{R}_0 T}\right)\prod_{i\in S}\left(c_i^0\right)^{\nu_{r,i}}, \tag{53}$$

where the reference molar concentration at standard pressure $P^0 = 1\,\mathrm{bar}$ defined as

- Gas species

$$c_i^0 = \frac{P^0}{\mathcal{R}T} \tag{54}$$

- Surface or bulk species in phase ω

$$c_i^0 = \frac{\Gamma_\omega}{\sigma_{\omega,i}}. \tag{55}$$

The change of molar Gibbs free energy during reaction is defined as

$$\Delta G_r = \sum_{i\in S} \nu_{r,i}\left(\overline{h}_i - T\,\overline{s}_i\right) + \mathcal{F} z \Delta\varphi, \tag{56}$$

where $\overline{h}_i$ and $\overline{s}_i$ are species molar enthalpy and entropy respectively.

3.4. Interface models

Interface models are responsible for the coupling between layers. Across different layers not only material properties but also governing equations and state variables can vary. Additionally, for 2D models layers may experience different extrusion along the unresolved third dimension.

The effective extrusion takes into account geometrical aspects of the cell, e.g. because of the finite thickness of channel and land the effective extrusion of the channel in z-direction is less than the extrusion of the cell for the 2D along-the-channel model geometry (see Fig. 5).

For an illustration of interface conditions consider domain (4) in Fig. 2, which is the interface between domains (1) and (2). In general an equal flux condition is applied

$$h_1\,\mathbf{f}_1\cdot\mathbf{n}^{1,4} \; + \; h_2\,\mathbf{f}_2\cdot\mathbf{n}^{2,4} = 0, \tag{57}$$

where $\mathbf{f}_1$ and $\mathbf{f}_2$ are flux terms in Eqs. (19) through (23). The weight h_1 and h_2 are relative extrusion factors for domain (1) and (2), which are related to physical extrusion of both adjacent domains through

$$\frac{h_1}{h_2} = \frac{H_1}{H_2}. \tag{58}$$

3.4.1. Velocity coupling

At the interface two state variables are taken into account: velocity on the left v_1 and on the right v_2 to the interface. The first condition compares their values, i.e.

$$h_1\,\mathbf{v}_1\cdot\mathbf{n}^{1,4} \; + \; h_2\,\mathbf{v}_2\cdot\mathbf{n}^{2,4} = 0. \tag{59}$$

Eq. (59) follows from the mass continuity at the boundary $A_1\rho_1\mathbf{v}\cdot\mathbf{n}^{1,4} + A_2\rho_2\mathbf{v}_2\cdot\mathbf{n}^{2,4} = 0$, where A_1 and A_2 are physical interface area from the left and from the right of the interface.

If Darcy–Brinkman equation (see Table 1) is present in both domains Eq. (57) provides an additional velocity criterion.

3.4.2. Species coupling

While a fluid phase assumes per default convection and diffusion of species, other phases (bulk and interface) may not include species transport. If a species is a subject of transport processes, Eq. (57) is applied. If chemical processes are taking place at the interface, the Eq. (57) can be extended to

$$h_1\,\mathbf{f}_1\cdot\mathbf{n}^{1,4} \; + \; h_2\,\mathbf{f}_2\cdot\mathbf{n}^{2,4} = \overline{q}_j, \tag{60}$$

where $\overline{q}_j$ is the interface chemical source of species j.

If a species i has no flux a zero gradient is imposed from both sides of the interface

$$\mathbf{n}^{1,4}\cdot\nabla c_i = \mathbf{n}^{2,4}\cdot\nabla c_i = 0. \tag{61}$$

3.5. Boundary models

The boundary conditions depend on the model geometry. For 1D geometry, concentrations of gas species, temperature and thus pressure are set at both electrode/channel interfaces. Additionally potential or current density are applied at the boundaries. In 2D either through or along configurations can be used (see Fig. 6). Along channel the isothermal no-slip boundary is assumed, whereby the gas channel assumes the electric conductivity of the land and respectively electric potential or current density boundary conditions are applied. Other boundaries assume adiabatic walls, except gas channels, were inflow and outflow boundary conditions are set. In general the model considers the following seven types of boundaries, which can be chosen depending on the configuration.

---

[3]

$$E_r^* = E_r + \alpha^*\, \mathcal{F} z_r \Delta\varphi \; - \; \sum_{j\in S} \epsilon_{r,j}\theta_j, .$$

3.5.1. *Isothermal wall*

For Darcy–Brinkman Eq. (18) the no-slip boundary condition is assumed, i.e.

$$\mathbf{v} = 0, \tag{62}$$

For the mass conservation a zero pressure gradient is assumed, i.e.

$$\mathbf{n} \cdot \nabla p = 0, \tag{63}$$

which zeros the velocity in the direction of normal vector to the boundary for the Darcy formulation.

In the case of species concentrations it is realised as follows.

1. The governing equation for main fluid species $i_{\max}$, the species which has the largest concentration at the beginning of the Newton iterations, is replaced by Eq. (63).
2. Other gas species $i \in \mathrm{g}$ are governed at the boundary by zero gradient of mole fraction X_i, i.e.

   $$\mathbf{n} \cdot \nabla X_i = 0, \quad \forall\ i \in \mathrm{g}, \tag{64}$$

   or with the units of molar concentrations c_i

   $$\mathbf{n} \cdot \left(\nabla c_i - \frac{c_i}{c} \nabla c \right) = 0, \quad \forall\ i \in \mathrm{g},\ i \neq i_{\max}, \tag{65}$$

   where $c = \sum_{j \in \mathrm{g}} c_j$ is the molar concentration of the fluid phase.

The isothermal condition implies that

$$T = T(t, \mathbf{x}_b), \tag{66}$$

whereby the temperature at the boundary can be a function of time t and boundary coordinates $\mathbf{x}_b$. In this case the Eq. (63) can be simplified to

$$\mathbf{n} \cdot \left(\frac{\partial p}{\partial c} \nabla c + \frac{\partial p}{\partial T} \nabla T \right) = 0. \tag{67}$$

Ionic and electronic potentials, and species from phases other than fluid, are subjects to zero flux condition, except electric current at the current collectors (see Section 3.5.7), i.e.

$$\mathbf{f} \cdot \mathbf{n} = 0, \tag{68}$$

where $\mathbf{f}$ is the flux term in Eqs. (21), (22) and (23).

3.5.2. *Adiabatic wall*

The boundary condition for an adiabatic wall is constructed similar to the isothermal wall by imposing zero velocity and zero pressure gradient at the boundary (see Eqs. (62) and (63) respectively). The adiabatic condition implies that

$$\mathbf{n} \cdot \nabla T = 0, \tag{69}$$

which simplifies Eq. (67) to

$$\mathbf{n} \cdot \nabla c_i = 0, \quad \forall\ i \in \mathrm{g}. \tag{70}$$

The Eq. (70) is the boundary condition for the species in the fluid phase.

For species other than fluid phase and for potentials Eq. (68) is valid.

3.5.3. *Inflow model*

At the gas inlet, velocity and gas species concentrations are imposed:

- Velocity

  $$\mathbf{v} = -\mathbf{n}\, v_0(t), \tag{71}$$

- Energy

  $$\mathbf{f} \cdot \mathbf{n} = v_0 \sum_{i \in \mathrm{g}} \bar{h}_i c_i, \tag{72}$$

- Species in the fluid phase

  $$\mathbf{f} \cdot \mathbf{n} = v_0\, c_i, \quad \forall\ i \in \mathrm{g}, \tag{73}$$

- Other species and potentials

  $$\mathbf{f} \cdot \mathbf{n} = 0, \tag{74}$$

where $v_0 = v_0(\mathbf{x_b})$ is the magnitude of the inflow velocity.

3.5.4. *Through channel boundary*

In the case of 2D through configuration the channel is not explicitly modelled (see Fig. 6) but different boundary conditions are set under channel and land:

Gas species

$$\begin{cases} c_i = c_i^0, & \forall z \in \text{channel}, \\ \mathbf{n} \cdot \left(\mathbf{v} \varepsilon_{\mathrm{g}} c_i + \bar{\mathbf{j}}_i \right) = 0, & \forall z \in \text{land}. \end{cases} \tag{75}$$

Electronic potential

$$\begin{cases} \mathbf{n} \cdot \mathbf{i}_{\mathrm{el}} = 0, & \forall z \in \text{channel}, \\ \varphi_{\mathrm{el}} = \varphi_{\mathrm{el}}^0, & \forall z \in \text{land}. \end{cases} \tag{76}$$

Temperature

$$T = T^0, \tag{77}$$

For other primary variables the flux through the boundary is set to zero.

3.5.5. *Darcy outflow model*

The outflow boundary condition refers only to the fluid phase. For species not in the fluid phase and for both potentials a zero flux is assumed, i.e. $\mathbf{f} \cdot \mathbf{n} = 0$.

Darcy outflow boundary condition imposes the pressure p_∞ at the outflow, i.e.

$$\begin{aligned} & p = p_\infty, \\ & \mathbf{n} \cdot \left(\nabla c_i - X_i \nabla c \right) = 0, \quad \forall\ i \in \mathrm{g},\ i \neq i_{\max}, \\ & \mathbf{n} \cdot \nabla T = 0, \end{aligned} \tag{78}$$

where $i_{\max}$ is the index of the species with the largest molar concentration at the beginning of the Newton iterations.

3.5.6. *Darcy-Brinkman outflow model*

There are two possible implementations of the outflow boundary condition for Darcy–Brinkman model: reflecting and non-reflecting.

Reflecting outflow imposes Darcy outflow Eq. (78) and fixes the flow velocity as

$$\begin{aligned} & \rho\, \mathbf{v} \cdot \nabla (\mathbf{v} \cdot \mathbf{n}) + \mathbf{n} \cdot \nabla p = 0, && \text{normal} \\ & \mathbf{e}_k^{\mathrm{b}} \cdot \mathbf{v} = 0, && \text{tangential}, \end{aligned} \tag{79}$$

where $\mathbf{n}$ normal vector to boundary and $\mathbf{e}_k^{\mathrm{b}}$ is boundary coordinate vector k.

Non-reflecting outflow model is based on Navier–Stokes Characteristic Boundary Condition (NSCBC), see [37] for more details. The model is summarised in Table 3. Eqs. (80) ans (81) in the table refer to storage $\mathbf{s}_{\mathrm{v}}$, flux $\mathbf{F}_{\mathrm{v}}$ and source $\mathbf{q}_{\mathrm{e}}$ terms for momentum conservation from Eq. (18). Eq. (82) refers to storage s_{e}, flux $\mathbf{f}_{\mathrm{e}}$ and source q_{e} terms for energy conservation from Eq. (19). Species outflow relies on storage s_i, flux $\mathbf{f}_i$ and source q_i terms for species conservation from Eq. (20).

Additionally, the NSCBC model requires local speed of sound and the mach number. The speed of sound is defined as

$$a = \sqrt{\left(\frac{\bar{c}_{\mathrm{p}}}{\bar{c}_{\mathrm{p}} - \mathcal{R}} \right) \frac{p}{\rho}}, \tag{84}$$

where $\bar{c}_{\mathrm{p}}$ is the molar heat capacity at constant pressure.

Mach number is defined as

$$\mathcal{M} = \frac{\sqrt{\mathbf{v} \cdot \mathbf{v}}}{a}. \tag{85}$$

Table 3
Summary of NSCBC model for fluid phase.

Flow velocity normal to boundary $\mathbf{n}\cdot\mathbf{v}$	
$\frac{\partial}{\partial t}\left(\mathbf{n}\cdot\mathbf{s}_{\mathrm{v}}\right)+\sum_{i=1}^{N^{\mathrm{b}}_{\mathrm{dim}}}\frac{\partial}{\partial x^{\mathrm{b}}_i}\left(\mathbf{e}^{\mathrm{b}}_i\cdot\mathbf{F}_{\mathrm{v}}\cdot\mathbf{n}\right)=\varepsilon_{\mathrm{g}}\mathbf{n}\cdot\left(\mathbf{g}\rho-\mathbf{v}\frac{\varepsilon_{\mathrm{g}}\,\mu}{K}\right)-\varepsilon_{\mathrm{g}}\left(d_1\,\mathbf{n}\cdot\mathbf{v}+d_3\,\rho\right)$	(80)
Flow velocity in the direction of boundary coordinates $\mathbf{e}^{\mathrm{b}}_k\cdot\mathbf{v}$	
$\frac{\partial}{\partial t}\left(\mathbf{e}^{\mathrm{b}}_k\cdot\mathbf{s}_{\mathrm{v}}\right)+\sum_{i=1}^{N^{\mathrm{b}}_{\mathrm{dim}}}\frac{\partial}{\partial x^{\mathrm{b}}_i}\left(\mathbf{e}^{\mathrm{b}}_i\cdot\mathbf{F}_{\mathrm{v}}\cdot\mathbf{e}^{\mathrm{b}}_k\right)=\mathbf{e}^{\mathrm{b}}_k\cdot\mathbf{q}_{\mathrm{v}}-\varepsilon_{\mathrm{g}}\left(d_1\,\mathbf{e}^{\mathrm{b}}_k\cdot\mathbf{v}+\rho\,(\mathbf{n}\cdot\mathbf{v})\left(\mathbf{n}\cdot\nabla\mathbf{e}^{\mathrm{b}}_k\mathbf{v}\right)\right)$	(81)
Energy outflow	
$\frac{\partial}{\partial t}s_{\mathrm{e}}+\sum_{i=1}^{N^{\mathrm{b}}_{\mathrm{dim}}}\frac{\partial}{\partial x^{\mathrm{b}}_i}\left(\mathbf{e}^{\mathrm{b}}_i\cdot\mathbf{f}_{\mathrm{e}}\right)=q_{\mathrm{e}}-\varepsilon_{\mathrm{g}}\left[d_1\left(h+\frac{1}{2}\mathbf{v}\cdot\mathbf{v}\right)+(\mathbf{n}\cdot\mathbf{v})\left(\mathbf{n}\cdot\nabla\left(h+\frac{1}{2}\mathbf{v}\cdot\mathbf{v}\right)\right)\right]$	(82)
Outflow of species i	
$\frac{\partial}{\partial t}s_i+\sum_{i=1}^{N^{\mathrm{b}}_{\mathrm{dim}}}\frac{\partial}{\partial x^{\mathrm{b}}_i}\left(\mathbf{e}^{\mathrm{b}}_i\cdot\mathbf{f}_i\right)=q_i-\varepsilon_{\mathrm{g}}\left[d_1\frac{c_i}{\rho}+\rho\,\mathbf{n}\cdot\nabla\frac{c_i}{\rho}\right]$	(83)
NSCBC parameters	
$d_1=\frac{1}{2}\left(\mathcal{L}_1+\mathcal{L}_5\right),\quad d_3=\left(\mathcal{L}_5-\mathcal{L}_1\right)/(2\rho a),$ $\mathcal{L}_1=\frac{1}{2}\left(p-p_\infty\right)(1-\mathcal{M})\,a/L,\quad \mathcal{L}_5=(\mathbf{n}\cdot\mathbf{v}+a)\,(\mathbf{n}\cdot\nabla p+\rho a\,\mathbf{n}\cdot\nabla\mathbf{v}\cdot\mathbf{n})$	

The mass specific enthalpy of the gas mixture can be computed via the molar specific enthalpy of the species in the fluid phase g

$$h=\frac{1}{\rho}\sum_{i\in\mathrm{g}}\overline{h}_i c_i. \tag{86}$$

3.5.7. Current collector

For the electron transport two types of boundary conditions can be applied to the electrode layers at the current collector boundaries. One can either impose the potential at the boundary

$$\varphi^{\mathbf{b}}_{\mathbf{e}}=\varphi_0(t), \tag{87}$$

or the current

$$\mathbf{i}^{\mathbf{b}}_{\mathbf{e}}=-\mathbf{n}\,i_0(t). \tag{88}$$

Typically, for the fuel electrode (87) with zero potential is applied

$$\varphi^{\mathbf{b}}_{\mathbf{e}}=0,$$

and for the air electrode either Eqs. (87) or (88) are applied for potentiostatic or galvanostatic operations respectively.

4. Applications

In this section two exemplary applications of the NEOPARD-X v. 2.0 framework are presented. One is a model for the proton exchange membrane fuel cell (PEMFC) and the other one is for a high temperature solid oxide electrolyser cell (SOEC). Models of different dimensionality are considered.

The examples were chosen to illustrate the framework capabilities. For this reason, although having a realistic behaviour, these models are simplified and they were not validated with experimental data. Detailed cell models with experimental validation are beyond the scope of the framework presentation and will be presented in dedicated future publications.

4.1. Polymer electrolyte membrane fuel cell

As a first application example of the framework we consider a simplified model for the polymer electrolyte membrane fuel cell (PEMFC). We will use this example to discuss the effect of model geometry, i.e., comparing 1D, 2D through-channel and 2D along-the-channel setups (cf. Fig. 6). For simplicity of presentation the example is limited to a single phase flow.

4.1.1. Model description

The PEMFC model uses the basic transport equations for mass, charge and energy as described above. The membrane electrode assembly (MEA) consists of seven layers (GDLs, MPLs, catalyst layers at both anode and cathode and the membrane) which are spatially resolved. The corresponding equations and layer thicknesses are summarised in Table 4. In addition, in case of the along-the-channel configuration transport in the MEA is coupled with free flow inside the gas channels (18). For the basic setup the cell geometry is based on the Baltic qCf 12 High Amp cell [38], i.e. the channel length is 4 cm, channel heights are 0.25 mm for the cathode and 0.17 mm for the anode. Channel and rib widths are 0.6 mm and 0.24 mm, respectively. In the following we introduce the equations specific for the PEMFC model, i.e. the reaction kinetics and transport properties.

The hydrogen oxidation reaction (HOR) is described by a Butler–Volmer kinetics (42) with the kinetic parameters based on Stühmeier et al. [39], $\alpha=0.5$, $i_0=0.52\frac{\mathrm{A}}{\mathrm{cm}^2}$, $\beta_{\mathrm{H}_2}=0.6$, $U_{0,\mathrm{HOR}}=0\,\mathrm{V}$.

For the oxygen reduction reaction (ORR) an analytical approximation is used according to [40] to solve the ionomer film model equation

$$k a^{\gamma}_{\mathrm{Pt}}+\left(a_{\mathrm{Pt}}-a_{\mathrm{eq}}\right)\frac{C_{\mathrm{ref}}}{R_{\mathrm{film}}}=0, \tag{89}$$

with reaction order $\gamma=0.8$, local ionomer film resistance $R_{\mathrm{film}}=1200\frac{\mathrm{s}}{\mathrm{m}}$ and reference concentration $C_{\mathrm{ref}}=34.5\frac{\mathrm{mol}}{\mathrm{m}^3}$.

Here, we use a modified Tafel kinetics taking into account the effect of platinum oxide coverage θ

$$k=i_0(1-\theta)\exp\left(-\frac{\omega\theta}{\mathcal{R}T}\right)\exp\left(-\frac{\alpha F\eta}{\mathcal{R}T}\right), \tag{90}$$

$$i_0=4Fk_0\exp\left(-\frac{E_{\mathrm{act}}}{\mathcal{R}}\left(\frac{1}{T}-\frac{1}{323.0\,\mathrm{K}}\right)\right), \tag{91}$$

where $\alpha=0.5$, $\omega=3\cdot10^3$ J and $k_0=80\ \mathrm{mol/m}^2_{\mathrm{Pt}}$, $E_{\mathrm{act}}=42\,\mathrm{kJ}$. The platinum oxide surface coverage is calculated according to [41] as

$$\theta=\frac{\exp\left(\frac{\alpha_{\mathrm{a}}F}{RT}\eta_{\mathrm{PtOx}}\right)}{\exp\left(\frac{\alpha_{\mathrm{a}}F}{RT}\eta_{\mathrm{PtOx}}\right)+\exp\left(\frac{-\alpha_{\mathrm{c}}F}{RT}\eta_{\mathrm{PtOx}}\right)}, \tag{92}$$

with $\alpha_{\mathrm{a}}=\alpha_{\mathrm{c}}=0.4$ and $U^0_{\mathrm{PtOx}}=0.86$ V. The overpotential of the platinum oxidation is defined as

$$\eta_{\mathrm{PtOx}}=\phi_{\mathrm{e}^-}-\phi_{\mathrm{H}^+}-U^0_{\mathrm{PtOx}}. \tag{93}$$

Similarly the overpotential η is defined for the ORR with the temperature-dependent equilibrium voltage

$$U^0_{\mathrm{ORR}}=1.23-9.0\cdot10^{-4}(T-298.15\,\mathrm{K}) \tag{94}$$

The source term for water production by the ORR at the cathode is split into two terms describing the fraction of water production within the ionomer and within the pore space, i.e.,

$$q_{\mathrm{ORR,pore}}=(1-\xi)\frac{j}{2F}, \tag{95}$$

and

$$q_{\mathrm{ORR,ionomer}}=\xi\frac{j}{2F}. \tag{96}$$

Here, we assume $\xi=0.03$.

The total source term for water in the ionomer (see Eq. (24)) is the sum of the water production by the ORR and the water sorption

$$q_\lambda=q_{\mathrm{ORR,ionomer}}+q_{\mathrm{sorp}}, \tag{97}$$

where the water sorption rate is defined by

$$q_{\mathrm{sorp}}=\frac{\varepsilon_\alpha k_\lambda}{L_{\mathrm{CCL}}}\frac{\rho_{\mathrm{dry}}}{\mathrm{EW}}\left(\lambda_{\mathrm{eq}}-\lambda\right), \tag{98}$$

with the equilibrium water content calculated according to [42]

$$\lambda_{\mathrm{eq}}=\begin{cases}\left(6.932a_{\mathrm{H2O}}-14.53a^2_{\mathrm{H2O}}+11.82a^3_{\mathrm{H2O}}\right) & \\ \quad\times\exp\left(-2509\left(\frac{1}{T}-\frac{1}{303.15}\right)\right), & \forall\ a_{\mathrm{H2O}}<1\\ 22, & \forall\ a_{\mathrm{H2O}}\geq1.\end{cases} \tag{99}$$

The sorption kinetics [43] is given by

$$k_\lambda = a_{\mathrm{sorp}} f_{\mathrm{V}} \exp\left[\frac{E_{\mathrm{ads}}}{\mathcal{R}}\left(\frac{1}{303\,\mathrm{K}} - \frac{1}{T}\right)\right], \tag{100}$$

with

$$f_{\mathrm{V}} = \frac{\lambda V_{\mathrm{H2O}}}{V_{\mathrm{m}} + \lambda V_{\mathrm{H2O}}}, \tag{101}$$

where V_{H2O} and V_{m} are the molar volume fractions of water and dry membrane, respectively, and

$$\begin{cases} a_{\mathrm{sorp}} = 1.14 \times 10^{-5}\,\frac{\mathrm{m}}{\mathrm{s}}, & \forall\ \lambda < \lambda_{\mathrm{eq}}, \\ a_{\mathrm{sorp}} = 4.5 \times 10^{-5}\,\frac{\mathrm{m}}{\mathrm{s}}, & \forall\ \lambda > \lambda_{\mathrm{eq}}. \end{cases} \tag{102}$$

Water transport in the ionomer/PEM is described by (24). The electroosmotic drag coefficient is calculated as [1]

$$n_{\mathrm{d}} = \frac{2.5\lambda}{22}. \tag{103}$$

For the water diffusion coefficient within the membrane many different parametrisations can be found in the literature [44]. Here, we use the formulation proposed by Kosakian et al. [42]. In the ionomer of the catalyst layers the diffusion coefficient is given by

$$D_\lambda = \frac{\partial \ln a_{\mathrm{H2O}}}{\partial \ln \lambda} D_i, \tag{104}$$

where the first term is the Darken factor

$$\frac{\partial \ln a_{\mathrm{H2O}}}{\partial \ln \lambda} = \begin{cases} \exp\left(0.7647\tilde{\lambda}^{2.305}\right), & \forall\ \tilde{\lambda} < 1.209; \\ 3.266 + 2.930\left[\exp\left(-6.735\,\frac{\tilde{\lambda} - 1.209}{\tilde{\lambda}^{0.8994}}\right) - 1\right], & \\ & \forall\ \tilde{\lambda} \geq 1.209, \end{cases} \tag{105}$$

with

$$\tilde{\lambda} = \lambda \exp\left[2509\left(\frac{1}{T} - \frac{1}{303.15\,\mathrm{K}}\right)\right] \tag{106}$$

and

$$D_i = 5.44 \cdot 10^{-9} f_{\mathrm{V}} \exp\left[\frac{20000}{\mathcal{R}}\left(\frac{1}{303\,\mathrm{K}} - \frac{1}{T}\right)\right]\frac{\mathrm{m}^2}{\mathrm{s}} \tag{107}$$

is the intradiffusion coefficient.

For the PEM the water diffusion coefficient is calculated as [42]

$$D_\lambda = \begin{cases} 9.92 \cdot 10^{-3}\lambda\left(\exp(0.28\lambda) - 1\right)\exp\left[-\frac{2436}{T}\right], & \\ & \forall\ 0 < \lambda \leq 3; \\ 13.344 \cdot 10^{-4}\lambda\left(161\exp(-\lambda) + 1\right)\exp\left[-\frac{2436}{T}\right], & \\ & \forall\ \lambda > 3, \end{cases} \tag{108}$$

Proton conductivity in the membrane is calculated according to [45] as

$$\sigma_{\mathrm{H+}} = 50.0\exp\left[\frac{15000}{\mathcal{R}}\left(\frac{1}{303.15\,\mathrm{K}} - \frac{1}{T}\right)\right]\left(f_{\mathrm{V}} - 0.06\right)^{1.5}\frac{\mathrm{S}}{\mathrm{m}}. \tag{109}$$

The same relation is used for the ionomer in the catalyst layers except for multiplication with a Bruggeman correction taking into account the ionomer volume fraction.

Energy transport is described by (19) and consists of the enthalpy transport due to mass transport as well as heat conduction. The species enthalpies are calculated using NASA polynomials while for the different layers constant effective heat conductivities are assumed as listed in Table 4.

The average inlet gas velocity is calculated based on the stoichiometry $\lambda_{\mathrm{O_2}}$ as

$$v_{\mathrm{air,in}} = \begin{cases} \lambda_{\mathrm{O_2}}\frac{A_{\mathrm{cell}}}{A_{\mathrm{channel}}}\frac{i}{4F\,c_{\mathrm{O_2}}}, & \forall\ i > i_{\mathrm{min}}, \\ \lambda_{\mathrm{O_2}}\frac{A_{\mathrm{cell}}}{A_{\mathrm{channel}}}\frac{i_{\mathrm{min}}}{4F\,c_{\mathrm{O_2}}}, & \forall\ i \leq i_{\mathrm{min}}, \end{cases} \tag{110}$$

Similar equations are used for the anode side. Pressure is imposed at the outlet (cf. Eq. (78)). Dirichlet boundary conditions are set for the temperature at the channel boundaries.

4.1.2. Results

Full 3D simulations of the fuel cell are very computationally demanding. Therefore, typically PEMFC models of lower dimension (2D or even 1D) are considered in literature. 1D models resolving the dimension through the MEA are often used to simulate the performance of PEMFC, e.g., in system models due to their fast computation time. However, these models neglect the effects occurring in the other two dimensions (along the channel and channel-land). 2D along-the-channel models in addition resolve the dimension along the gas channels, while 2D through-the-channel or channel-land models resolve the perpendicular dimension, distinguishing between channel and land regions. When using these models of reduced dimension, gradients along the unresolved dimensions are neglected or have to be taken into account by modified boundary conditions. It is therefore important to verify the validity of these simplifying assumptions. In our framework the physical model equations within the cell are decoupled from the actual model geometry, allowing for easy variation from 1D to 2D through- or along-the-channel setup. In the following the effect of model dimension is discussed with respect to variations in stoichiometry, relative humidity and channel/land widths.

In the first study, the effect of stoichiometry $\lambda_{\mathrm{O_2}}$ is investigated. For the along-the-channel model, stoichiometry affects the inlet velocity according to (110). On the other hand, for the 1D and 2D through-the-channel geometry gas concentrations have to be set at the GDL/channel boundary. The simplest assumption is to use the inlet concentrations, i.e., neglecting concentration gradients along the channel and therefore the effect of stoichiometry. Fig. 7 a) and b) show the comparison of the three model geometries for cathode stoichiometry $\lambda_{\mathrm{O_2}}$ of 2 and 10 for relative humidity (RH) of 50% and 80%, respectively. The temperature is set to 80 °C and the outlet pressure to 2.5 bar in all simulations. Obviously, in this case the stoichiometry only affects the along-the-channel model as it does not enter the other two setups. Compared to the 1D and the through-the-channel model, under dry conditions the along-the-channel model yields higher cell voltages in the intermediate current region, while transport limitations are reached earlier, depending on the stoichiometry. Only at very low currents up to approx. $0.1\ \mathrm{A/cm^2}$ all setups provide similar results under these conditions. The earlier transport limitations are caused by the oxygen concentration decreasing along the channel, while the higher performance in the intermediate current range is due to increasing water content along the channel and therefore better ionomer and membrane humidification. Note, that the differences to the 1D case are still significant even at very high stoichiometries of 10 as they are used, e.g., in differential cells. This is due to the parabolic velocity profile inside the channel, which leads to significant concentration gradients along the GDL/channel interface even at high stoichiometries. On the other hand, the difference between through-the-channel and 1D geometry are quite small and only relevant close to the limiting current. Under well humidified conditions shown in Fig. 7 b) all three model geometries yield quite similar cell performance as long as transport limitations are negligible. Also in this case, transport limitations occur first in the along-the-channel setup. Thus, based on this study it is more important to resolve the dimension along the channel as transport limitations under the land are less relevant (cf. also Fig. 8). This holds at least for the cell geometry considered here, which is based on the Baltic qCf 12 High Amp cell with quite thin land width of 0.24 mm at the cathode. One might expect that the channel-land effect becomes more relevant at cell designs with larger land width. Fig. 7 c) shows the effect of increasing land width while the channel width is kept constant at 0.6 mm. Indeed, increasing the land widths leads to a significant decrease of the limiting current. Thus, for cells with larger land widths of ≥ 0.5 mm operated at

Table 4
Configuration of PEMFC model.

Layer	Unknowns	Submodels	Thickness µm	λ_{ef} $\frac{W}{m\,k}$	Phase	ε	τ	K $10^{-12}m^2$
1. GDL	$T,\ \varphi_{el},$	(17), (19),	74	0.3	Gas	$0.74\ \frac{m^3}{m^3}$	1.3	1.0
	$c_{H_2(g)},\ c_{H_2O(g)}$	(20), (23)			Carbon	$0.26\ \frac{m^3}{m^3}$		
2. MPL	$T,\ \varphi_{el},$	(17), (19),	76	0.3	Gas	$0.61\ \frac{m^3}{m^3}$	1.7	0.47
	$c_{H_2(g)},\ c_{H_2O(g)}$	(20), (23)			Carbon	$0.39\ \frac{m^3}{m^3}$		
3. ACL	$T,\ \varphi_{el},\ \varphi_{ion},$	(17), (19),	4	0.2	Gas	$0.55\ \frac{m^3}{m^3}$	1.2	0.001
	$c_{H_2(g)},\ c_{H_2O(g)},$	(20), (21),			Carbon	$0.26\ \frac{m^3}{m^3}$		
	λ	(22), (23),			Ionomer	$0.19\ \frac{m^3}{m^3}$		
		(24)			Carbon|Ionomer	$2.12 \cdot 10^7\ \frac{m}{m^2}$		
4. PEM	$T,\ \varphi_{ion},\ \lambda,\ c_{H_2O}$	(19), (22), (21), (24)	14	0.15	Ionomer	$1\ \frac{m^3}{m^3}$		
5. CCL	$T,\ \varphi_{el},\ \varphi_{ion},$	(17), (19),	6	0.2	Gas	$0.55\ \frac{m^3}{m^3}$	1.2	0.001
	$c_{H_2(g)},\ c_{H_2O(g)},$	(20), (21),			Carbon	$0.26\ \frac{m^3}{m^3}$		
	$c_{O_2(g)},\ c_{N_2(g)}$	(22), (23),			Ionomer	$0.19\ \frac{m^3}{m^3}$		
	λ	(24)			Carbon|Ionomer	$2.98 \cdot 10^7\ \frac{m}{m^2}$		
6. MPL	$T,\ \varphi_{el},\ c_{H_2O(g)},$	(17), (19),	76	0.3	Gas	$0.61\ \frac{m^3}{m^3}$	1.7	0.47
	$c_{H_2(g)},\ c_{O_2(g)},\ c_{N_2(g)}$	(20), (23)			Carbon	$0.39\ \frac{m^3}{m^3}$		
7. GDL	$T,\ \varphi_{el},\ c_{H_2O(g)},$	(17), (19),	74	0.3	Gas	$0.74\ \frac{m^3}{m^3}$	1.3	1.0
	$c_{H_2(g)},\ c_{O_2(g)},\ c_{N_2(g)}$	(20), (23)			Carbon	$0.26\ \frac{m^3}{m^3}$		

large stoichiometries, indeed the channel-land dimension can become decisive in the limiting current region.

In the simulations discussed so far, the channel inlet oxygen concentration was used as boundary condition for the 1D and through-the-channel geometries. Compared to the along-the-channel model this leads to an overestimation of the limiting current. As an alternative approach one might consider to modify the concentration at the boundary, taking into account the concentration gradients along the channel. The outlet concentration can be calculated based on the stoichiometry. With the respective fluxes of oxygen and nitrogen at inlet and outlet

$$\begin{aligned}
F_{O_{2,in}} &= X_{O_{2,in}} \frac{p_{dry}}{\mathcal{R}T} v_{in} = \lambda_{O_2} \frac{A_{cell}}{A_{channel}} \frac{i}{4\mathcal{F}}, \\
F_{N_{2,in}} &= \left(1 - x_{O_{2,in}}\right) \frac{p_{dry}}{\mathcal{R}T} v_{in}, \\
F_{O_{2,out}} &= X_{O_{2,out}} \frac{p_{dry}}{\mathcal{R}T} v_{out} = \left(1 - \lambda_{O_2}\right) \frac{A_{cell}}{A_{channel}} \frac{i}{4\mathcal{F}}, \\
F_{N_{2,out}} &= \left(1 - X_{O_{2,out}}\right) \frac{p_{dry}}{\mathcal{R}T} v_{out},
\end{aligned} \tag{111}$$

and $F_{N_{2,in}} = F_{N_{2,out}}$ one obtains the oxygen mole fraction at the outlet

$$X_{O_{2,out}} = \frac{\left(\lambda_{O_2} - 1\right) X_{O_{2,in}}}{\lambda_{O_2} - X_{O_{2,in}}}. \tag{112}$$

Fig. 7 d) shows the 1D model using an average oxygen mole fraction $\left(X_{O_{2,in}} + x_{O_{2,out}}\right)/2$ as alternative boundary condition for the case $\lambda_{O_2} = 2$. As one can see, the limiting current still is overestimated compared to the along-the-channel model. This is due to the parabolic velocity profile inside the channels and the consequent strongly non-linear oxygen concentration profile along the channel (cf. Fig. 8 a)). Indeed, a significantly lower oxygen concentration than the average is needed ($X_{O2,optim} = 0.134$ in this example) in order to obtain the correct limiting current. However, in this case the cell voltage over the whole range of current densities gets already significantly underestimated. Thus, modifying the oxygen boundary condition does not allow for an accurate description of the cell behaviour in a 1D model. Instead, modifications of the cathode oxygen transport properties would be needed in order to capture the correct limiting current in 1D. However, when doing so, one has to keep in mind that the used model will no longer reflect the real physical processes in the cell as along-the-channel effects are spuriously assigned to through-the-MEA concentration gradients.

To conclude this part, at sufficiently low currents all model geometries yield similar results. This can be helpful for model parametrisation since all properties relevant in this region (e.g. ORR kinetics) could be parametrised using a fast 1D model. In the intermediate current region, 1D models can still be quite accurate especially for well humidified conditions while under dry conditions the occurring strong gradients in water content along the channel are neglected in 1D, which lead to significant deviations from the along-the-channel model. The limiting current region cannot be accurately described by the 1D model when using the correct physical transport properties, as gradients along the channel are important in this region and cannot be neglected. The gradients occurring in channel-land dimension are less relevant compared to the ones along the channel, at least for sufficiently thin land widths used in current state-of-the-art test cells. For cells with large land widths operated at high stoichiometry through-channel models can be used. At low stoichiometry, gradients in all three spacial dimensions become relevant which requires full 3D simulations.

4.2. High temperature steam electrolysis

As a second example a SOEC model for steam electrolysis with an exemplary 4 × 4 cm^2 cell is used. The model has 11 layers (including channels) with different physical properties and different state variables. Here, an along-the-channel 2D configuration (see Fig. 6) is chosen to illustrate the capabilities of the framework with respect to impedance simulation and the extension from cell to stack models.

4.2.1. Model description

The model contains 11 layers as summarised in Table 5. The current collector boundary conditions are assigned to layers 2 and 9. Both channels have inflow and outflow boundary conditions and other layers have adiabatic wall boundary conditions. Consider Tables 5 through 8 for the detailed list of model parameters, applied equations and unknowns (primary variables) in each layer. The concentration of defects c_{V_O} in YSZ and CGO is computed from the site density in the bulk material Γ, i.e.:

$$\mathrm{V_O} = \Gamma - c_{O^{2-}}, \tag{113}$$

where $\Gamma = \Gamma_{CGO}$ or $\Gamma = \Gamma_{YSZ}$, depending on the layer.

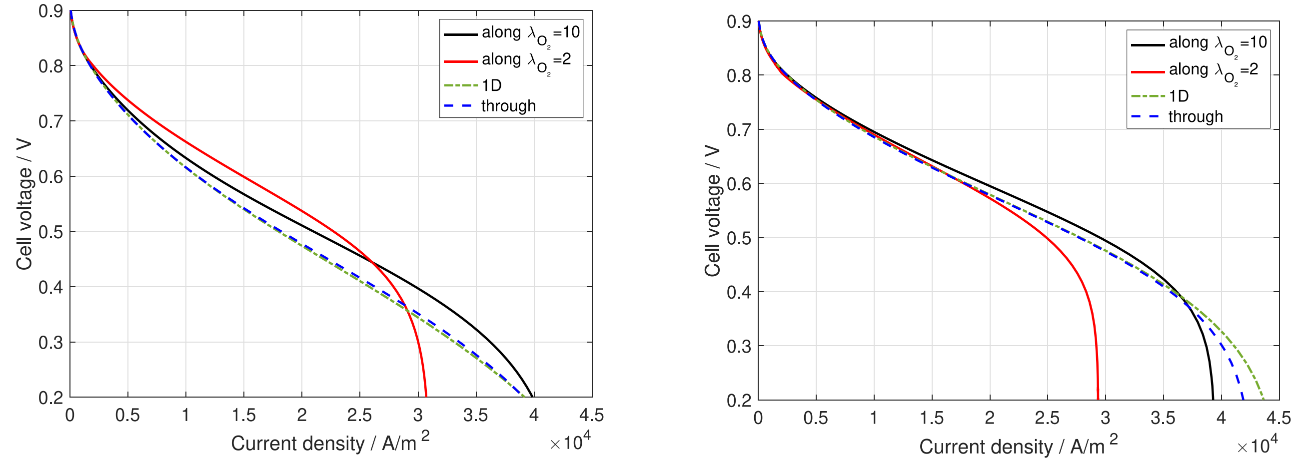

(a) Comparison along-the-channel, through-channel and 1D model for 50% RH

(b) Comparison along-the-channel, through-channel and 1D model for 80% RH

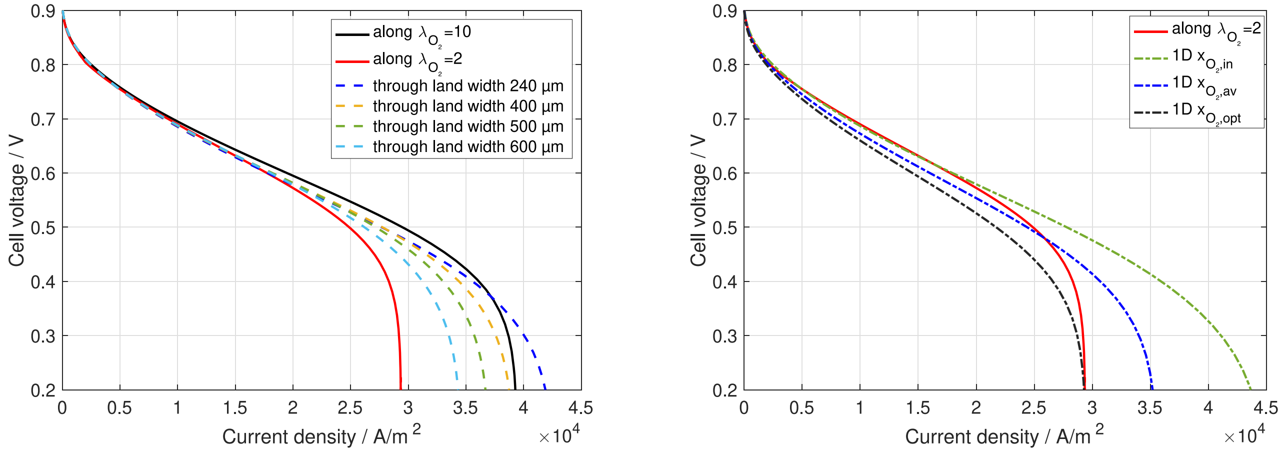

(c) Effect of land width in through-channel model

(d) Effect of oxygen boundary condition in 1D model

Fig. 7. Effects of model geometry on the polarisation curves.

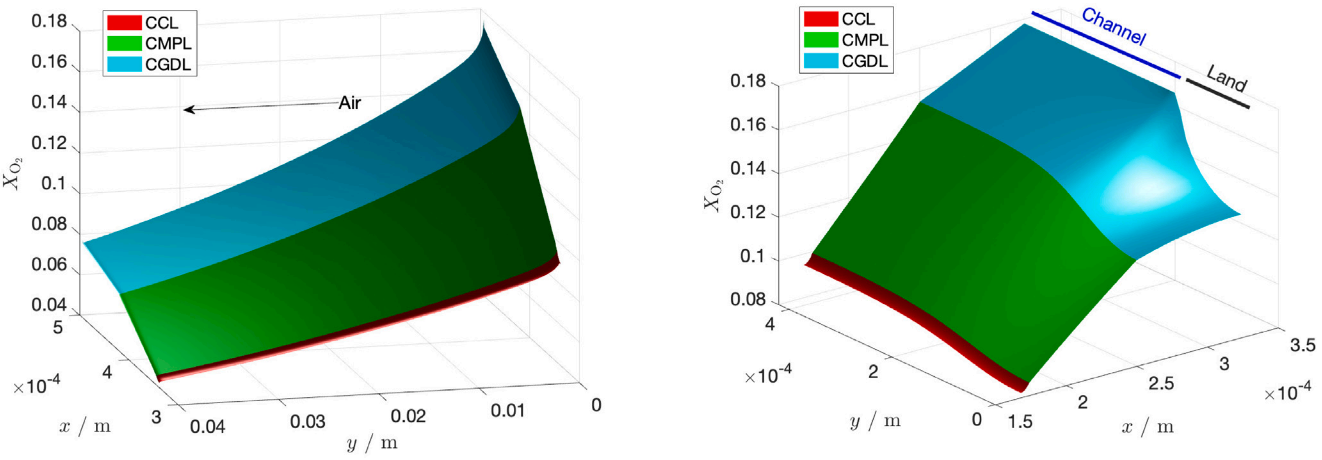

(a) Along channel for $\lambda_{O_2} = 2$

(b) Through channel

Fig. 8. Comparison of the oxygen distribution for different 2D geometries at the respective limiting currents for 80% RH.

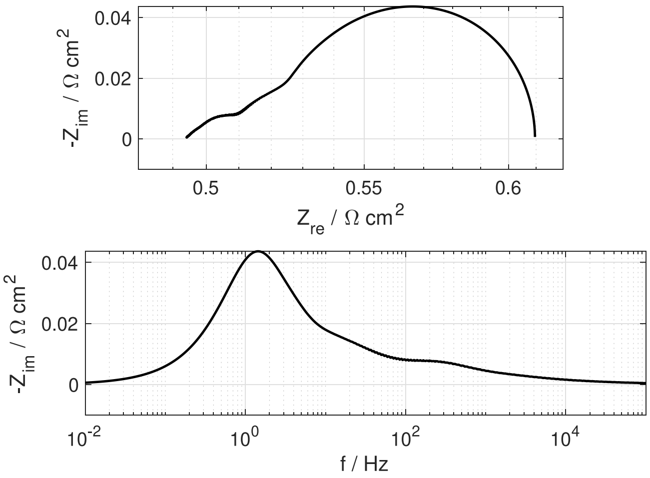

Fig. 9. SOEC impedance at OCV for binary 50% H_2 and 50% H_2O mixture at T = 860 °C.

Cell boundaries are assumed adiabatic, see Eqs. (69) and (70). Channel inflow and outflow boundary conditions are described by Eqs. (71), (72), (73), (74) and Eqs. (80), (81), (82), (83) respectively.

4.2.2. Results

The proposed transient model cannot only be used to simulate polarisation curves but any electrochemical characterisation method such as e.g. electrochemical impedance spectroscopy. This can be very helpful for model validation, as impedance spectroscopy provides additional information about the time scales of the processes. On the other hand, a physical model can help in correctly interpreting the impedance spectra by identifying and quantifying the underlying physical processes.

A typical impedance, resulting from the SOEC model without electrical load is shown in Fig. 9. Here the peak around f = 3 Hz results mostly from the gas conversion along the channel. It is overlapped with a small peak from the reaction (R2) (refer to Table 8). The peak around f = 20 Hz comes from the oxygen reduction reaction (R1) and process around f = 300 Hz relates to the surface electro-chemical reaction (R3). The time required for computing the full impedance is about 2 min on Intel i7 CPU with 6 cores.

In order to illustrate 2D effects during steam electrolysis, several representative profiles are shown in Fig. 10. These profiles represent the equilibrium state for T = 860 °C, current load of i = 1.6 A/cm^2, O_2/N_2 = 21/79 air composition and H_2/H_2O = 50/50 fuel molar composition. Due to the near complete steam utilisation (compare Fig. 10(d)), one can observe an increase in air channel flow velocity by 20% (see Fig. 10(a)).

The cell model can also be easily extended to a stack model, by linking several cells with bipolar plates. Fig. 11 shows temperature profiles for a short stack with 5 cells. Each cell is described by the same model as described above. The bipolar plate is a simple electron conducting layer made of steel, i.e. only electronic potential and thermal fields are resolved according to Eqs. (19), (23). To the authors knowledge, a SOEC stack model with the presented physical complexity within each cell has not yet been reported in literature. It only becomes computationally feasible due to the efficient parallelisation of the code (cf. Section 4.3).

The most noticeable difference between single cell and the stack is the temperature increase. The temperature increase at the moderate cell voltage of 1.6 V is for a single cell less than 1 K but for a short stack of 5 cells is already about 6 K (compare Figs. 10(b) and 11(b)).

The computation time of a single cell SOEC model with 48 cores (single node) at HPC JUSTUS2 is about 7.5 min and of a short stack of 5 cells about 23 min. The size of models (the total number of unknowns) is 65’604 and 269’148 respectively. To the authors best knowledge, there are no frameworks capable of computing cell stacks with comparable model complexity.

4.3. Numerical performance

As an illustration of the numerical performance of the framework, it is shown how the duration of the computational scales with the number of cores, and how the accuracy improves with the increase of grid point density. For the benchmark high-performance computers (HPC) were used: HPE Apollo (HAWK) at Stuttgart HLRS and BwForCluster JUSTUS2. JUSTUS2 is based on Intel® Xeon E6252 and HAWK is utilising AMD® EPYC 7742 processors. As a linear system solver the Intel® oneAPI PARDISO library was used, as it is readily available on both clusters as a module.

The scalability of the computational time with increase of number of processing cores is illustrated by Fig. 13 as applied to the PEMFC model with 2D along channel configuration. The model has 16’116 grid points and 105’198 unknowns in total. Performance test were run on clusters HAWK and JUSTUS2. Here, the computational time with one core serves as the reference τ_{ref}. The overall computational time (black lines) is split into two components: the time required by NEOPARD-X for processing the model (blue) and the time required by an external library for the solution of the linear system (red). For a comparison of real computational times the reader is referred to Table 9.

The model computation in NEOPARD-X shows near linear scalability till 64 cores, which is improved for larger systems. The circles in Fig. 13 represents the reference grid with 16’116 grid points and 105’198 unknowns; crosses show the performance for double resolution in x and y directions, i.e. 48’711 grid points and 308’938 unknowns; and triangles show the quadruple resolutions with 169’101 grid points and 1’052’418 unknowns. Although the model computation scales similarly on HAWK and JUSTUS2 HPC, the overall performance scales better on JUSTUS2. This has two reasons:

1. Linear solver is better scaled on JUSTUS2. The Intel® oneAPI PARDISO is probably better optimised for Intel processors compared to AMD processors used in HAWK.
2. The model computation time on JUSTUS2 is about 5 times longer than on HAWK, while the linear solver time is approximately the same.

The limited scalability for a large number of cores by the computation of the model is most likely attributed to memory copy operations from NEOPARD-X to PARDISO storage.

4.4. Numerical convergence

The numerical convergence is demonstrated with the SOEC model but it is similar for the PEMFC model. In order to reduce the number of required grid points the Sigmoid stretching is applied (see Section 2.5.1). In the current setup sigmoid parameters $a_1 = 0.1$, $b_1 = 0.5$, $a_2 = 0.05$ and $b_2 = 0.5$ are used for all layers.

Consider Fig. 12, which shows an error estimation with respect to a reference solution.

$$E_i = \max_{\mathbf{x}} \left| \frac{U_i(\mathbf{x}) - U_{\text{ref}}(\mathbf{x})}{U_{\text{ref}}(\mathbf{x})} \right|. \tag{114}$$

The reference solution U_{ref} is constructed from the basis solution U_1 by increasing the number of points by the factor 8 for each coordinate direction. The basis solution is constructed with a minimal number of points. The coordinate in Fig. 12 corresponds to the increase in the number of grid points with respect to the basis solution U_1. In order to illustrate the convergence, computed error estimations are fitted by

$$E = \frac{\alpha}{n^{\beta}}, \tag{115}$$

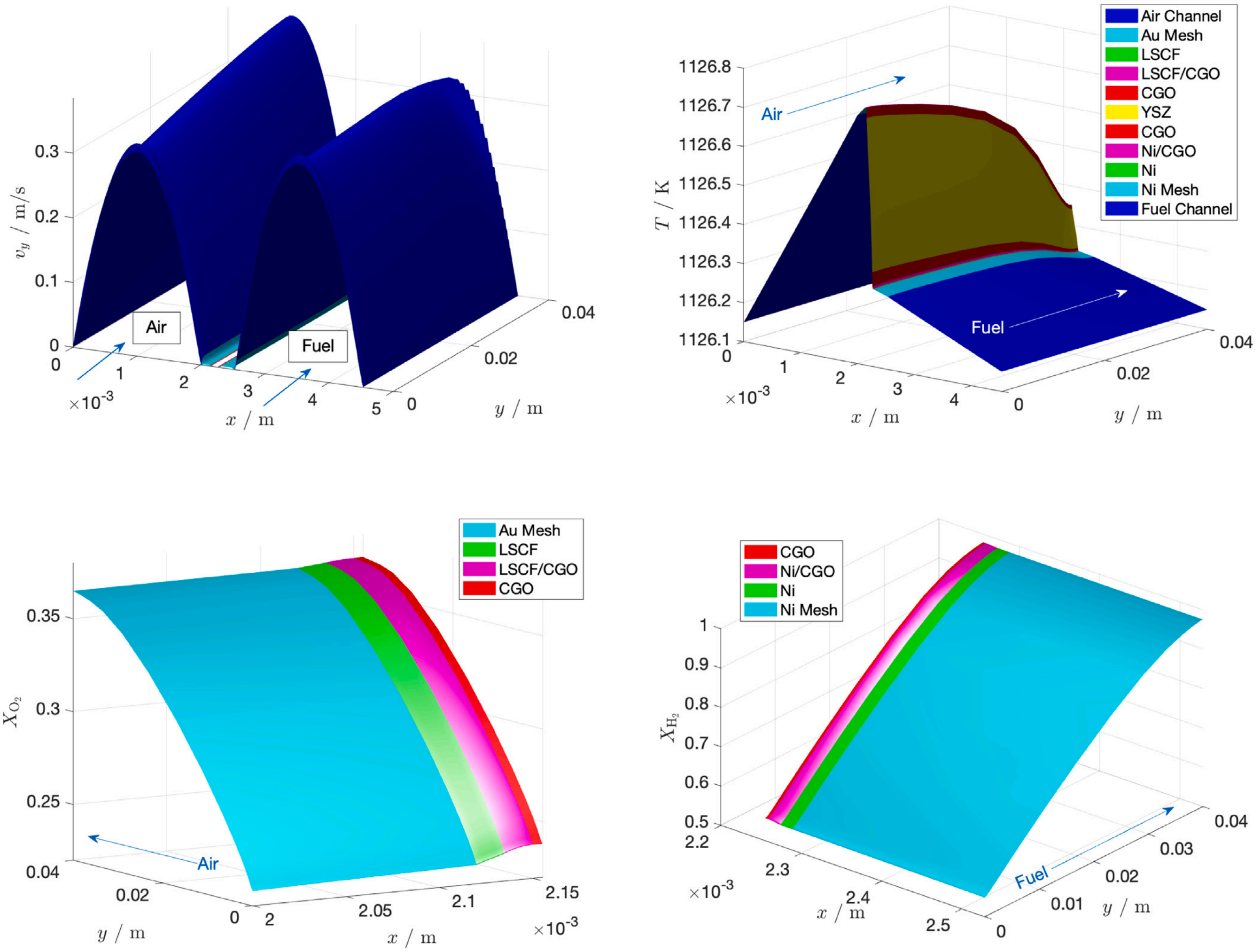

(c) mole fraction of oxygen

(d) mole fraction of hydrogen

Fig. 10. SOEC equilibrium profiles for cell voltage of 1.6 V at $T = 860\,^{\circ}\mathrm{C}$ with 50% H_2 and 50% H_2O fuel composition.

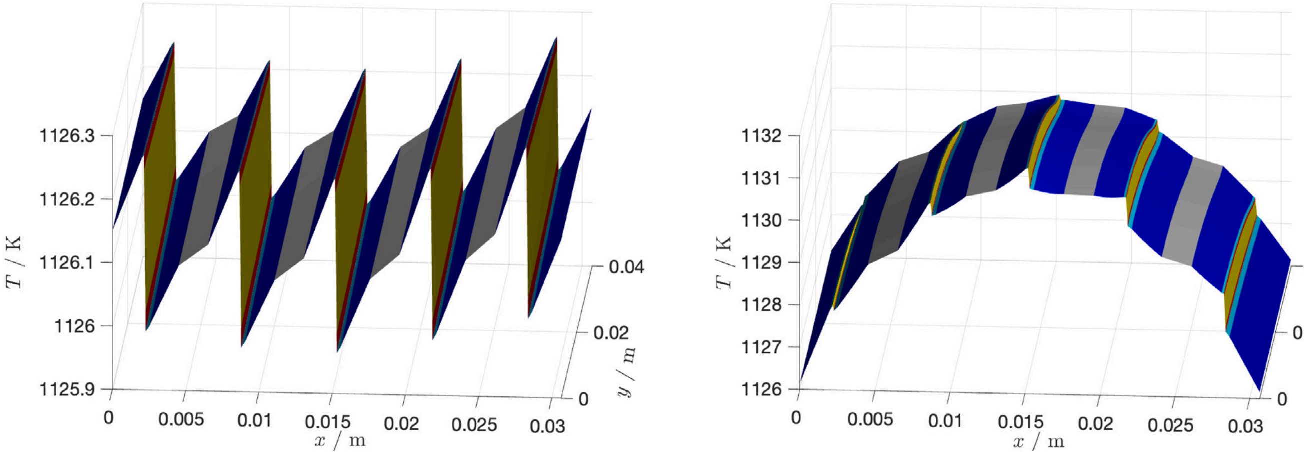

(a) Thermoneutral point (1.3 V)

(b) Cell voltage 1.6 V

Fig. 11. SOEC Short Stack temperature profiles for water electrolysis with 50% H_2 and 50% H_2O in the gas feed. Bipolar plates are shown in grey, for cell colour description see Fig. 10.

Table 5
Configuration of SOEC model.

Layer	Unknowns	Submodels	Width µm	C_{dl} MF/m^3	Phase	ε	τ	K m^2
1. Air channel	$\mathbf{v}$, T, $c_{O_2(g)}$, $c_{N_2(g)}$	(18), (19), (20)	2000		Air	$1\ \frac{m^3}{m^3}$	1	∞
2. Gold mesh	$\mathbf{v}$, T, φ_{el},	(18), (19),	120		Air	$0.85\ \frac{m^3}{m^3}$	1.1	2.2×10^{-10}
	$c_{O_2(g)}$, $c_{N_2(g)}$	(20), (23)			Au	$0.15\ \frac{m^3}{m^3}$	1.1	
3. LSCF	$\mathbf{v}$, T, φ_{el},	(18), (19),	15		Air	$0.4\ \frac{m^3}{m^3}$	1.5	5.8×10^{-16}
	$c_{O_2(g)}$, $c_{N_2(g)}$	(20), (23)			LSCF	$0.6\ \frac{m^3}{m^3}$	1.5	
4. LSCF/CGO	T, φ_{el}, φ_{ion},	(17), (19),	15	350	Air	$0.4\ \frac{m^3}{m^3}$	1.5	3.4×10^{-16}
	$c_{O_2(g)}$, $c_{N_2(g)}$,	(20), (21),			LSCF	$0.25\ \frac{m^3}{m^3}$	1.5	
	$c_{O^{2-}}$,	(22), (23)			CGO	$0.35\ \frac{m^3}{m^3}$	1.5	
	$c_{O(g\|CGO)}$				Air|LSCF|CGO	$5 \cdot 10^{12}\ \frac{m}{m^3}$		
5. CGO	φ_{el}, φ_{ion}, $c_{O_2(g)}$,	(17), (19), (20),	5		Air	$0.4\ \frac{m^3}{m^3}$	1.3	3.7×10^{-16}
	T, $c_{N_2(g)}$, $c_{O^{2-}}$	(21), (22), (23)			CGO	$0.6\ \frac{m^3}{m^3}$	1.3	
6. YSZ	T, φ_{ion}, $c_{O^{2-}}$	(19), (21), (22)	100		YSZ	$1\ \frac{m^3}{m^3}$		
7. CGO	φ_{el}, φ_{ion}, $c_{H_2(g)}$,	(17), (19), (20),	5		Fuel	$0.4\ \frac{m^3}{m^3}$	1.3	3.8×10^{-16}
	T, $c_{H_2O(g)}$, $c_{O^{2-}}$	(21), (22), (23)			CGO	$0.6\ \frac{m^3}{m^3}$	1.3	
8. Nickel/CGO	T, φ_{el}, φ_{ion},	(17), (19),	12	40	Fuel	$0.4\ \frac{m^3}{m^3}$	1.7	2.9×10^{-16}
	$c_{H_2(g)}$, $c_{H_2O(g)}$,	(20), (21),			Nickel	$0.35\ \frac{m^3}{m^3}$	1.7	
	$c_{O^{2-}}$,	(22), (23)			CGO	$0.25\ \frac{m^3}{m^3}$	1.7	
	$c_{O(g\|CGO)}$				Fuel|CGO	$8 \cdot 10^{7}\ \frac{m^2}{m^3}$		
9. Nickel	$\mathbf{v}$, T, φ_{el},	(18), (19),	12		Fuel	$0.5\ \frac{m^3}{m^3}$	1.2	1.3×10^{-12}
	$c_{H_2(g)}$, $c_{H_2O(g)}$	(20), (23)			Nickel	$0.5\ \frac{m^3}{m^3}$	1.2	
10. Nickel Mesh	$\mathbf{v}$, T, φ_{el},	(18), (19),	240		Fuel	$0.6\ \frac{m^3}{m^3}$	1.2	2.2×10^{-10}
	$c_{H_2(g)}$, $c_{H_2O(g)}$	(20), (23)			Nickel	$0.4\ \frac{m^3}{m^3}$	1.2	
11. Fuel channel	$\mathbf{v}$, T, $c_{H_2(g)}$, $c_{H_2O(g)}$	(18), (19), (20)	2000		Fuel	$1\ \frac{m^3}{m^3}$	1	∞

Table 6
Phase properties at $T = 860$ °C.

Phase	Site density Γ	Intern. Energy U	Heat cond. λ/ W/m/K	Electr. cond. σ_e/ S/m
Air[a]	10.68 mol/m^3	177.3 kJ/m^3	0.077	0
Fuel[b]	10.68 mol/m^3	1.09 MJ/m^3	0.234	0
LSCF	34568 mol/m^3	17.79 GJ/m^3	116.0	96.0×10^3
CGO	10000 mol/m^3	88.34 GJ/m^3	2.140	0.045
YSZ	46714 mol/m^3	2.82 MJ/m^3	1.938	0
Gold	98000 mol/m^3	12.25 GJ/m^3	246.0	45.5×10^6
Nickel	151770 mol/m^3	5.87 MJ/m^3	74.5	2.19×10^6
Air|LSCF|CGO	4.5×10^{-15} mol/m	0	0	0
Fuel|CGO	1.36×10^{-5} mol/m	0	0	0

[a] Reference values computed for 21% O_2, 79% N_2 and $p = 1$ bar.
[b] Reference values computed for 50% H_2, 50% H_2O and $p = 1$ bar.

Table 7
Species properties at $T = 860$ °C.

Phase	Species	Charge z	Enthalpy $\bar{h}$/ kJ/mol	Entropy $\bar{s}$/ J/mol/K
Air[a]	O_2(g)	–	27.2	247.7
	N_2(g)	–	25.6	232.0
Fuel[a]	H_2(g)	–	24.5	169.7
	H_2O(g)	–	−210.5	237.6
CGO[b]	O^{2-}	−2	−201	70
YSZ[c]	V_O	0	0	0
Fuel|CGO[c]	O(g|CGO)	0	−158.0	0
	CGO(g|CGO)	0	0	0

[a] Computed from NIST-JANAF tables: https://janaf.nist.gov.
[b] Taken from the Ref. [46].
[c] Estimated.

where β represents the slope and thus the order of convergence. The resulting rate of convergence is $\beta = 2.2 \pm 0.2$, with lowest value $\beta = 2.0$ for temperature and the highest value $\beta = 2.4$ for mole fractions of steam and hydrogen. As expected, the FCFVM shows a second order convergence in respect to grid points, although the grid points are distributed inequidistantly in physical space (see Section 2.5.1).

5. Conclusion

The new NEOPARD-X v. 2.0 framework for electro-chemical modelling of electrolyser and fuel cells is presented. The framework combines detailed models of the involved fundamental physical and chemical processes. It includes the following features:

1. The framework is applicable for computation of stationary (e.g. polarisation curves) and for fully transient studies (e.g. electrochemical impedance).
2. Within the framework models from 0D to 3D can be implemented.
3. Model development is separated from the discretisation, which facilitates extension of existing models and introduction of new sub-models to the framework.
4. The framework is parallelised for shared memory architectures, which makes accessible the computation of complex physical models for short stacks, computationally demanding degradation simulations and detailed 3D computations. This is an essential feature for future simulation-based optimisation and virtual design of fuel cell and electrolyser technologies.
5. The use of either detailed elementary kinetics or Butler–Volmer formulation is possible. Charge transfer reactions, heterogeneous (double phase or triple phase boundary) reactions and gas-phase reactions are treated thermodynamically consistently.

Table 8
Reaction parameters at $T = 860\ °\mathrm{C}$.

Phase	Reaction	Rate[a]	
Air|LSCF|CGO	$\frac{1}{2}\,O_2(g) + V_O + 2\,e^- \rightleftharpoons O^{2-}$	$A = 4.5 \times 10^{-10}\ \frac{m^3}{mol^{1/2}\ s}$	(R1)
Fuel|CGO	$H_2O(g) + CGO(g\|CGO) \rightleftharpoons O(g\|CGO) + H_2(g)$	$A = 0.6 \times 10^{1}\ \frac{m^3}{mol\ s}$	(R2)
	$O(g\|CGO) + V_O + 2\,e^- \rightleftharpoons O^{2-} + CGO(g\|CGO)$	$A = 3.75 \times 10^{-4}\ \frac{m^3}{mol\ s}$	(R3)

[a] Arrhenius parameters E and b are assumed zero.

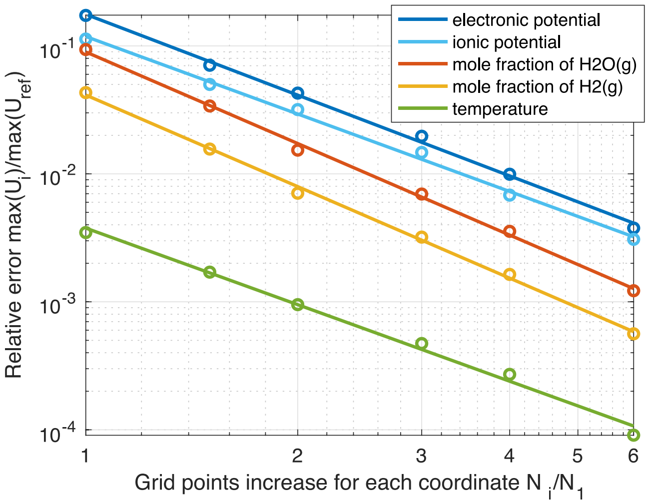

Fig. 12. Convergence of SOEC model: Circles are computed points, lines are linear fits.

Table 9
Computational time in seconds for PEMFC along model vs. number of processing cores.

N-CPU	1	2	4	8	16	32	48	64	128
JUSTUS 2 HPC									
Model	6569	3358	1682	867	431	235	183	–	–
PARDISO	402	269	189	155	155	141	149	–	–
HAWK HPC									
Model	1290	650	312	169	92	57	44	39	36
PARDISO	346	269	198	170	198	203	212	210	192

The modelling approach was illustrated with two examples: a model for a polymer electrolyte membrane fuel cell (PEMFC) and one for a solid oxide electrolyser cell (SOEC). The calculations provide insight into the effects of model dimensionality, potential and temperature distribution within the porous electrodes and the electrolyte, as well as the contribution of the model components to overall polarisation losses. Additionally the examples are used to illustrate the performance and the scalability of the framework.

The PEMFC model was used to compare three commonly used model geometries, i.e. 1D, 2D along-the-channel and 2D through-channel. At low currents all model geometries yield similar results, i.e. in this region using 1D models can be sufficient. In the intermediate current region, 1D models can still be quite accurate at least for well humidified conditions. However, under dry conditions gradients in water content along the channel become important which lead to significant deviations between the 1D and the along-the-channel model. The limiting current region cannot be accurately described by the 1D model as gradients along the channel are important in this region and cannot be neglected. Through-channel models are applicable especially for cells with large land widths operated at high stoichiometry.

The SOEC model was chosen to illustrate the transient solution for computation of impedances and to show the elementary kinetics approach for modelling of electro-chemical processes. Additionally the single cell SOEC model was scaled to a short stack of 5 cells, without altering the cell model. The computation time of only 23 min for the short stack demonstrates the capabilities of the framework for simulating highly complex models.

The model performance was tested on high performance computers HAWK at HLRS and JUSTUS 2 at bwHPC. In all cases a nearly linear scalability in respect to number of cores was observed, which is essential for more complex models. By overcoming the current bottleneck for the data transfer between the numerical framework and external linear solver, the scalability is prospected to improve even further in the near future.

Current applications were studied with face centred finite volumes method (FCFVM). However, other discretisation methods can be implemented with the framework. It was demonstrated that with the help of domain transformation the method remains second order even for inequidistant grids in physical domain.

CRediT authorship contribution statement

Andrey Koksharov: Writing – original draft, Visualization, Validation, Investigation, Conceptualization. **Arnulf Latz:** Supervision, Resources, Funding acquisition, Conceptualization. **Thomas Jahnke:** Writing – review & editing, Supervision, Project administration, Investigation, Funding acquisition.

Declaration of competing interest

The authors declare the following financial interests/personal relationships which may be considered as potential competing interests: Authors report a relationship with German Federal Ministry of Education and Research that includes: funding grants. Authors report a relationship with Horizon 2020 that includes: funding grants. If there are other authors, they declare that they have no known competing financial interests or personal relationships that could have appeared to influence the work reported in this paper.

Data availability

No data was used for the research described in the article.

Acknowledgements

The authors gratefully acknowledge funding by the German Federal Ministry of Education and Research (BMBF 03SFK2E0-2) within the Kopernikus Project P2X. Furthermore, this work has received funding from the Fuel Cells and Hydrogen 2 Joint Undertaking (now Clean Hydrogen Partnership) under grant agreement No. 875025 (FURTHER-FC). This Joint Undertaking receives support from the European Union's Horizon 2020 research and innovation program. The work has also received funding by the project PEMTASTIC which is supported by the Clean Hydrogen Partnership and its members Hydrogen Europe and Hydrogen Europe Research under the Grant Agreement 101101433. Additionally the authors thank the High Performance Computing Center Stuttgart (HLRS) through the grant LaBoRESys (HAWK cluster) and the state of Baden-Württemberg through bwHPC and the German Research Foundation (DFG) through grant no INST 40/575-1 FUGG (JUSTUS 2 cluster) for performing computations.

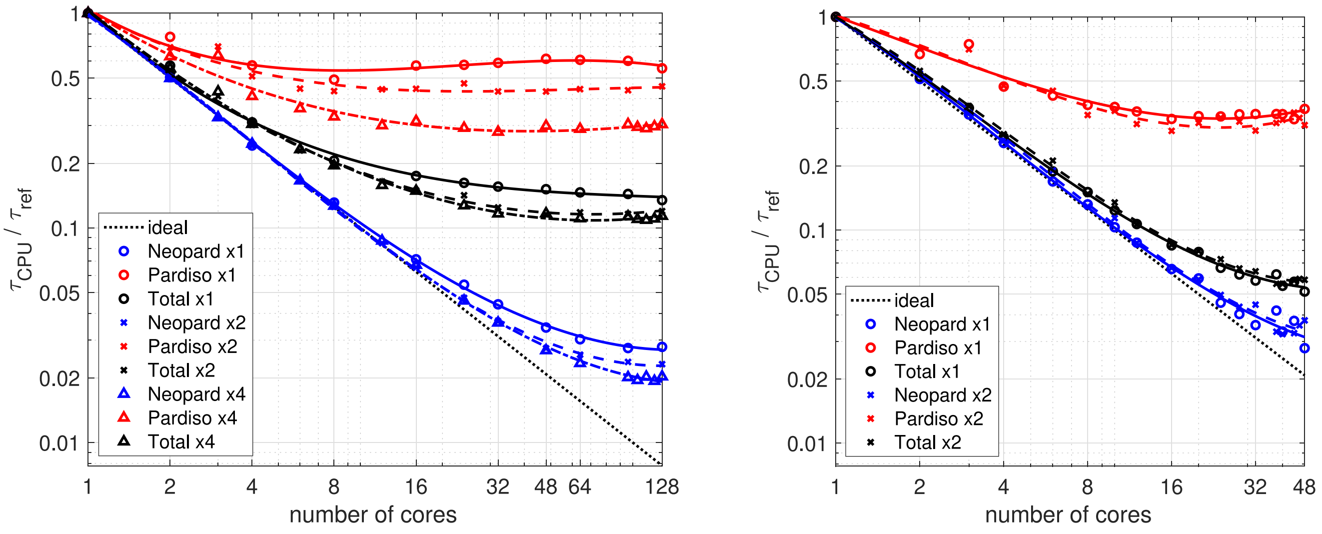

(a) HAWK

(b) JUSTUS 2

Fig. 13. Scalability on high performance computer: x1 — standard resolution, x2 — double resolution, x4 — quadruple resolution; lines are fits of the data.

Appendix A. Implementation of FCFV

The implemented FCFV method consists of two parts: interpolation between grid points and computation of integral values for finite volumes (quadrature rules). The computations are performed in coordinates ξ such that each component $\xi_i \in [0, 1]$ (see Section 2.5).

Interpolation

The interpolated value is computed linearly between adjacent grid points as shown in Fig. A.14. Please note that here boundary domains 3 and 4 have different discretisation as the main domain 0. Because during the computation the location of points is seldom changed, the interpolation routine (see Algorithm 1) provides a list of related points with corresponding coefficients. This list can be the used efficiently during the model integration for the value interpolation. The interpolation method is in general of O(1), but it becomes O(2) if the interpolation point is located exactly in the middle between the collocation points (rectangle in Fig. A.14). If the point lays near the boundary, firstly relations for virtual points are computed in the boundary domain, which are then used in the primary domain. In Fig. A.14 the interpolation relations are shown for inner point (red) and for a point near the boundary (magenta).

In the illustrated case (Fig. A.14) the red point depends only on 4 points, which lay within the domain 0, i.e. $R = \left\{ \left[\frac{1}{16}, u_5^0\right], \left[\frac{3}{16}, u_6^0\right], \left[\frac{3}{16}, u_9^0\right], \left[\frac{9}{16}, u_{10}^0\right] \right\}$. The dependency list of the magenta point extends to 5 points, i.e. $R = \left\{ \left[\frac{1}{8}, u_2^0\right], \left[\frac{3}{8}, u_3^0\right], \left[\frac{1}{32}, u_1^3\right], \left[\frac{9}{32}, u_2^3\right], \left[\frac{3}{16}, u_0^6\right] \right\}$. The latter points are computed iteratively by requesting relations of virtual points from boundary domains. The process is repeated till the corner point u_0^6 in domain 6 is reached. The coefficients in the above lists R correspond to coefficients $a_{i,j}^{m,k}$ in Eq. (3). The coefficients that are not listed are assumed 0.

Integration

FCFV treats Eq. (1) in weak form, which for single finite volume takes the following form:

$$\frac{\partial}{\partial t} \int_{\Omega} s \, \mathrm{d}V + \int_{\partial\Omega} \mathbf{f} \cdot \mathbf{n} \mathrm{d}S = \int_{\Omega} q \, \mathrm{d}V. \tag{A.1}$$

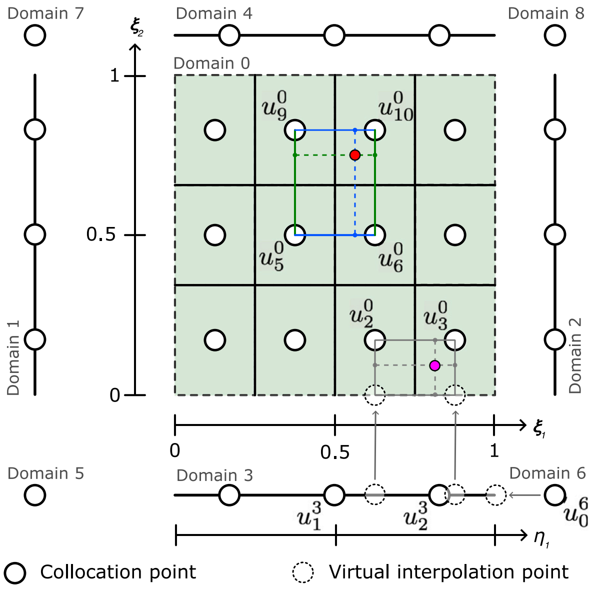

Fig. A.14. Interpolation with FCFV module.

Storage and source term integrals are approximated by the value in the centre of the volume (collocation points) and the flux terms are approximated by the value at the centre of the volume faces (blue points), see Fig. A.15:

$$\frac{\partial}{\partial t} \tilde{s}_i + \sum_{k \in K} \frac{A_{i,k}}{V_i} \tilde{\mathbf{f}}_{i,k} \cdot \mathbf{n}_{i,k} = \tilde{q}_i, \tag{A.2}$$

where $\tilde{s}_i$ and $\tilde{q}_i$, are approximation of the storage and source terms in the centre of the finite volume i, V_i is the volume and $A_{i,k}$ is area of the face k, $\tilde{\mathbf{f}}_{i,k} \cdot \mathbf{n}_{i,k}$ is the flux approximation through the face k.

Algorithm 1 Pseudo code for interpolation: N_k is the number of grid points in coordinate direction k, M is the number of dimensions, I is the set of all point indices in the current domain, ξ is the computational coordinate, η is the boundary computation coordinate. "BND.INTERP" refers to a call to interpolation within boundary domain.

```
function INTERP($\xi$, $k \leftarrow 0$, $w \leftarrow 1$)
    $i_k \leftarrow \left\lfloor \xi_k N_k - \frac{1}{2} \right\rfloor$
    $c_0 \leftarrow i_k - \xi_k N_k + \frac{3}{2}$
    $c_1 \leftarrow 1 - c_0$
    $R \leftarrow \{\}$
    for $j \in \{0, 1\}$ do
        if k == M-1 then
            if $i \notin I$ then
                $R \leftarrow R \cup$ BND.INTERP($\eta \leftarrow$ map($\xi$))
            else
                $R \leftarrow R \cup \left[w\, c_k, \mathrm{point}_i\right]$
            end if
        else
            $R \leftarrow R \cup$ INTERP($\xi$, $k+1$, $w\, c_j$)
        end if
    end for
    return $R$
end function
```

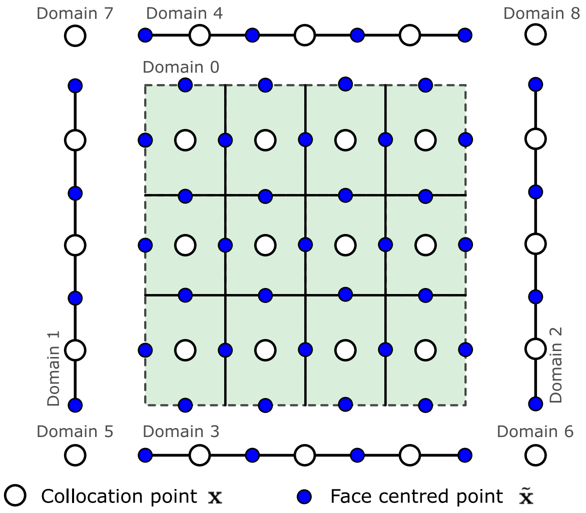

Fig. A.15. Integration with FCFV module.

References

[1] T.E. Springer, T.A. Zawodzinski, S. Gottesfeld, Polymer electrolyte fuel cell model, J. Electrochem. Soc. 138 (8) (1991) 2334.

[2] D.M. Bernardi, M.W. Verbrugge, A mathematical model of the solid-polymer-electrolyte fuel cell, J. Electrochem. Soc. 139 (9) (1992) 2477.

[3] A. Hirano, M. Suzuki, M. Ippommatsu, Evaluation of a new solid oxide fuel cell system by non-isothermal modeling, J. Electrochem. Soc. 139 (10) (1992) 2744.

[4] M. Tomberg, M.P. Heddrich, F. Sedeqi, D. Ullmer, S.A. Ansar, K.A. Friedrich, A new approach to modeling solid oxide cell reactors with multiple stacks for process system simulation, J. Electrochem. Soc. 169 (5) (2022) 054530.

[5] O. Babaie Rizvandi, X.-Y. Miao, H.L. Frandsen, Multiscale modeling of degradation of full solid oxide fuel cell stacks, Int. J. Hydrog. Energy 46 (54) (2021) 27709–27730.

[6] S. Gößling, N. Nickig, M. Bahr, 2-D + 1-D PEM fuel cell model for fuel cell system simulations, Int. J. Hydrog. Energy 46 (70) (2021) 34874–34882.

[7] J. Macedo-Valencia, J. Sierra, S. Figueroa-Ramírez, S. Díaz, M. Meza, 3D CFD modeling of a PEM fuel cell stack, Int. J. Hydrog. Energy 41 (48) (2016) 23425–23433.

[8] R. Vetter, J.O. Schumacher, Free open reference implementation of a two-phase PEM fuel cell model, Comput. Phys. Comm. 234 (2019) 223–234.

[9] B. Xie, G. Zhang, J. Xuan, K. Jiao, Three-dimensional multi-phase model of PEM fuel cell coupled with improved agglomerate sub-model of catalyst layer, Energy Convers. Manage. 199 (2019) 112051.

[10] R. Ma, F. Gao, E. Breaz, Y. Huangfu, P. Briois, Multidimensional reversible solid oxide fuel cell modeling for embedded applications, IEEE Trans. Energy Convers. 33 (2) (2018) 692–701.

[11] S.B. Beale, H.-W. Choi, J.G. Pharoah, H.K. Roth, H. Jasak, D.H. Jeon, Open-source computational model of a solid oxide fuel cell, Comput. Phys. Comm. 200 (2016) 15–26.

[12] U.R. Salomov, E. Chiavazzo, P. Asinari, Pore-scale modeling of fluid flow through gas diffusion and catalyst layers for high temperature proton exchange membrane (HT-PEM) fuel cells, Comput. Math. Appl. 67 (2) (2014) 393–411, Mesoscopic Methods for Engineering and Science (Proceedings of ICMMES-2012, Taipei, Taiwan, 23–27 July 2012).

[13] G. Wang, P.P. Mukherjee, C.-Y. Wang, Direct numerical simulation (DNS) modeling of PEFC electrodes: Part I. Regular microstructure, Electrochim. Acta 51 (15) (2006) 3139–3150.

[14] P. Sarkezi-Selsky, H. Schmies, A. Kube, A. Latz, T. Jahnke, Lattice Boltzmann simulation of liquid water transport in gas diffusion layers of proton exchange membrane fuel cells: Parametric studies on capillary hysteresis, J. Power Sources 535 (2022) 231381.

[15] A.Z. Weber, R.L. Borup, R.M. Darling, P.K. Das, T.J. Dursch, W. Gu, D. Harvey, A. Kusoglu, S. Litster, M.M. Mench, R. Mukundan, J.P. Owejan, J.G. Pharoah, M. Secanell, I.V. Zenyuk, A critical review of modeling transport phenomena in polymer-electrolyte fuel cells, J. Electrochem. Soc. 161 (12) (2014) F1254.

[16] K. Wang, D. Hissel, M. Péra, N. Steiner, D. Marra, M. Sorrentino, C. Pianese, M. Monteverde, P. Cardone, J. Saarinen, A review on solid oxide fuel cell models, Int. J. Hydrog. Energy 36 (12) (2011) 7212–7228.

[17] W.G. Bessler, S. Gewies, M. Vogler, A new framework for physically based modeling of solid oxide fuel cells, Electrochim. Acta 53 (4) (2007) 1782–1800.

[18] M. Secanell, A. Putz, P. Wardlaw, V. Zingan, M. Bhaiya, M. Moore, J. Zhou, C. Balen, K. Domican, OpenFCST: An open-source mathematical modelling software for polymer electrolyte fuel cells, ECS Trans. 64 (3) (2014) 655.

[19] D.B. Harvey, J.G. Pharoah, K.F. Karan, FAST-FC: Open source fuel cell model: An open source performance and degradation fuel cell model for PEMFCs, 2023, https://www.fastsimulations.com/source-code.html. (Accessed 11 August 2023).

[20] G.A. Futter, P. Gazdzicki, K.A. Friedrich, A. Latz, T. Jahnke, Physical modeling of polymer-electrolyte membrane fuel cells: Understanding water management and impedance spectra, J. Power Sources 391 (2018) 148–161.

[21] G.A. Futter, A. Latz, T. Jahnke, Physical modeling of chemical membrane degradation in polymer electrolyte membrane fuel cells: Influence of pressure, relative humidity and cell voltage, J. Power Sources 410–411 (2019) 78–90.

[22] T. Jahnke, G.A. Futter, A. Baricci, C. Rabissi, A. Casalegno, Physical modeling of catalyst degradation in low temperature fuel cells: Platinum oxidation, dissolution, particle growth and platinum band formation, J. Electrochem. Soc. 167 (1) (2019) 013523.

[23] T. Gießgen, T. Jahnke, Assisted cold start of a PEMFC with a thermochemical preheater: A numerical study, Appl. Energy 331 (2023) 120387.

[24] A. Quarteroni, R. Sacco, F. Saleri, Numerical mathematics, in: Texts in Applied Mathematics, Springer, New York, 2000.

[25] J.W. Demmel, J.R. Gilbert, X.S. Li, An asynchronous parallel supernodal algorithm for sparse Gaussian elimination, SIAM J. Matrix Anal. Appl. 20 (4) (1999) 915–952.

[26] G.A. Korn, T.M. Korn, Mathematical Handbook for Scientists and Engineers : Definitions, Theorems, and Formulas for Reference and Review, 2., enl. and rev. ed., in: McGraw-Hill Handbook, McGraw-Hill, New York, 1968.

[27] S. Mathur, P. Tondon, S. Saxena, Thermal conductivity of binary, ternary and quaternary mixtures of rare gases, Mol. Phys. 12 (6) (1967) 569–579.

[28] R.J. Kee, M.E. Coltrin, P. Glarborg, Chemically Reacting Flow: Theory and Practice, Wiley Interscience, Hoboken, NJ, 2003.

[29] W. Kast, C.-R. Hohenthanner, Mass transfer within the gas-phase of porous media, Int. J. Heat Mass Transfer 43 (5) (2000) 807–823.

[30] J.O. Hirschfelder, C.F. Curtiss, R.B. Bird, Molecular theory of gases and liquids, in: Structure of Matter Series, Wiley, New York, 1954.

[31] R.B. Bird, W.E. Stewart, E.N. Lightfoot, Transport Phenomena, revised 2nd, Wiley, New York, 2007.

[32] F.A. Williams, Combustion theory: the fundamental theory of chemically reacting flow systems, 2. ed., repr. with corr., in: Combustion Science and Engineering Series, Addison Wesley, Redwood City, Calif., 1988.

[33] P.W. Atkins, J. De Paula, J. Keeler, Atkins' Physical Chemistry, Oxford University Press, 2006.

[34] R. O'hayre, S.-W. Cha, W. Colella, F.B. Prinz, Fuel Cell Fundamentals, John Wiley & Sons, 2016.

[35] D. Chatterjee, O. Deutschmann, J. Warnatz, Detailed surface reaction mechanism in a three-way catalyst, Faraday Discuss. 119 (2002) 371–384.

[36] L. Maier, B. Schädel, K. Herrera Delgado, S. Tischer, O. Deutschmann, Steam reforming of methane over nickel: Development of a multi-step surface reaction mechanism, Top. Catalysis 54 (13) (2011) 845.

[37] T. Poinsot, S. Lele, Boundary conditions for direct simulations of compressible viscous flows, J. Comput. Phys. 101 (1) (1992) 104–129.

[38] U. Groos, M. Zedda, A. Casalegno, ID-FAST - Investigations on degradation mechanisms and Definition of protocols for PEM Fuel cells Accelerated Stress Testing D4.1: Definition of new reference single cell hardware, 2023, https://www.id-fast.eu/uploads/media/ID-FAST_D4-1_Definition_of_new_reference_single_cell_hardware_PUBLIC_OK.pdf. (Accessed 17 August 2023).

[39] B.M. Stühmeier, M.R. Pietsch, J.N. Schwämmlein, H.A. Gasteiger, Pressure and temperature dependence of the hydrogen oxidation and evolution reaction kinetics on pt electrocatalysts via PEMFC-based hydrogen-pump measurements, J. Electrochem. Soc. 168 (2021) 064516.

[40] T. Jahnke, A. Baricci, An analytical approximation for the ionomer film model in PEMFC, J. Electrochem. Soc. 169 (2022) 094514.

[41] W. Yoon, A.Z. Weber, Modeling low-platinum-loading effects in fuel-cell catalyst layers, J. Electrochem. Soc. 158 (8) (2011) B1007.

[42] A. Kosakian, L.P. Urbina, A. Heaman, M. Secanell, Understanding single-phase water-management signatures in fuel-cell impedance spectra: A numerical study, Electrochim. Acta 350 (2020) 136204.

[43] S. Ge, X. Li, B. Yi, I.-M. Hsing, Pabsorption, desorption, and transport of water in polymer electrolyte membranes for fuel cells, J. Electrochem. Soc. 152 (6) (2005) A1149.

[44] R. Vetter, J.O. Schumacher, Experimental parameter uncertainty in PEM fuel cell modeling Part I: Scatter in material parameterization, J. Power Sources 438 (2018) 227018.

[45] A.Z. Weber, J. Newman, Transport in polymer-electrolyte membranes : II. Mathematical model, J. Electrochem. Soc. 151 (2004) A311.

[46] V. Yurkiv, R. Costa, Z. Ilhan, A. Ansar, W.G. Bessler, Impedance of the surface double layer of LSCF/CGO composite cathodes: An elementary kinetic model, J. Electrochem. Soc. 161 (4) (2014) F480.